SUMMERTIME OZONE POLLUTION IN CHINA: OBSERVATIONS AND SIMULATIONS

A Dissertation
Presented to
The Academic Faculty

by

Hang Qu

In Partial Fulfillment
of the Requirements for the Degree
Doctor of Philosophy in the
School of Earth and Atmospheric Sciences

Georgia Institute of Technology
May 2020

SUMMERTIME OZONE POLLUTION IN CHINA: OBSERVATIONS AND SIMULATIONS

Approved by:

Dr. Yuhang Wang, Advisor
School of Earth and Atmospheric Sciences
Georgia Institute of Technology

Dr. Nga Lee (Sally) Ng
School of Chemical and Biomolecular Engineering
Georgia Institute of Technology

Dr. Lewis G. Huey
School of Earth and Atmospheric Sciences Engineering]
Georgia Institute of Technology

Dr. Jennifer Kaiser
School of Civil and Environmental Engineering
Georgia Institute of Technology

Dr. Rodney J. Weber
School of Earth and Atmospheric Sciences
Georgia Institute of Technology

Date Approved: March 11, 2020

ACKNOWLEDGEMENTS

I would like to express my greatest appreciation to my advisor, Dr. Yuhang Wang, without whose support and patient guidance I would not have been able to complete my research. I have been always inspired by his professional knowledge and insights throughout my Ph.D. I would also like to thank my Ph.D. thesis committee members, Dr Lewis G. Huey, Dr. Rodney J. Weber, Dr. Nga Lee (Sally) Ng, and Dr. Jennifer Kaiser for reviewing this thesis and their comments.

I would also like to thank the group members. I have had a great time working with Dr. Ja-Ho Koo, Dr. Yongjia Song, Dr. Dasa Gu, Dr. Yuzhong Zhang, Dr. Yufei Zou, Dr. Ruixiong Zhang, Dr. Jianfeng Li, Dr. Ye Cheng, Charles Smeltzer, Aoxing Zhang, Qiyang Yan, Kezhen Chong, Fanghe Zhao, and Shengjun Xi. I would specially thank Dr. Ruixiong Zhang as my roommate and my friend who helps me a lot with my research.

Finally, I would like to address my deepest and most sincere gratitude to my parents. It is their encouragements that I could move on at the most challenging time of my research.

TABLE OF CONTENTS

LIST OF TABLES

LIST OF FIGURES

LIST OF SYMBOLS AND ABBREVIATIONS

APS	Aerodynamic Particle Sizer
AQI	Air Quality Index
BC	Boundary Conditions
CAREBEIJING-NCP	Campaigns of Air Pollution Research in Megacity Beijing and North China Plain
CIMS	Chemical Ionization Mass Spectrometry
CMAQ	Community Multi-scale Air Quality
CNEMC	China National Environmental Monitoring Center
CRDS	Cavity Ring-down
CTMs	Chemical Transport Models
DOMINO	Dutch OMI NO_2
EKMA	Empirical Kinetic Modeling Approach
EMG	Exponentially Modified Gaussian
FID	Flame Ionization Detector
GC	Gas Spectrometer
GCM	GEOS-Chem mechanism
GEOS	Goddard Earth Observing System
GOME	Global Ozone Monitoring Experiment
IC	Initial Conditions
LIF	Laser-induced Fluorescence
LOPAP	Long-path Absorption Photometry
MCM	Master Chemical Mechanism
MDA8	Maximum Daily 8 hour Average

MEGAN	Model of Emissions of Gases and Aerosols from Nature
MEIC	Multi-resolution Emission Inventory for China
MIX	Model Inter-Comparison Study
MOZART	Model for Ozone and Related Chemical Tracers
MS	Mass Spectrometer
N:C	NOx to VOC
NCEP CFSv2	National Centers for Environmental Prediction Climate Forecast System Version 2
NCEP-FNL	National Centers for Environmental Prediction Final Analysis
NCP	North China Plain
NE	Northeast
NEI	National Emission Inventory
NMHCs	Non-Methane Hydrocarbons
NW	Northwest
OMI	Ozone Monitoring Instrument
OVOCs	Oxygenated VOCs
PAN	Peroxyacetyl Nitrate
PKU	Peking University
PM	Particular Matters
PRD	Pearl River Delta
RBL	Residual Boundary Layer
REAM	Regional chEmical transport Model
RH	Hydrocarbons
SMOKE	Sparse Matrix Operator Kernel Emissions
SOA	Secondary Organic Aerosol

SW	Southwest
TDMPS	Twin Differential Mobility Particle Sizer
TROPOMI	TROPOspheric Monitoring Instrument
UV	Ultraviolet
VOCs	Volatile Organic Compounds
WRF	Weather Research and Forecasting model
YRD	Yangtze River Delta

SUMMARY

High ozone concentrations have become the major summertime air quality problems in China. Extensive in situ observations are deployed for developing strategies to effectively control the emissions of ozone precursors, i.e., nitrogen oxides (NO_X=NO+NO_2) and volatile organic compounds (VOCs). The modeling analysis of in situ observations often makes uses of the dependence of ozone peak concentration on NO_X and VOC emissions, because ozone observations are among the most widely available air quality measurements. To extract more information from regulatory ozone observations, we extend the ozone-precursor relationship to ozone peak time. We find that the sensitivities of ozone peak time and concentration are complimentary for regions with large anthropogenic emissions such as China. For example, when ozone peak concentration is sensitive to VOC emissions but not to NO_X emissions, ozone peak time is sensitive to the latter. The extended ozone-precursor relationships can be readily applied to understand the effects on ozone by emission changes of NO_X and VOC and to assess potential biases of NO_X and VOC emission inventories. These observation constraints based on regulatory ozone observations can complement the other measurement and modeling analysis methods nicely. Furthermore, we suggest that the ozone peak time sensitivity we discussed here to be used as a model evaluation measure before the EKMA diagram is applied to understand the effectiveness of emission control on ozone concentrations.

We also make use of the extensive ozone observations in China to identify the resulting constraints of the nighttime mixing processes. Model simulated night-time ozone minima have a large low bias of up to 40 ppbv compared to the observations. We found

that the underestimated night-time vertical mixing over the urban areas is the most plausible explanation for the widespread high-level nocturnal ozone surface concentrations in China. Enhanced night-time vertical mixing from the surface to 200-500 meters in urban areas is necessary for the model to reproduce the observed surface ozone. The underestimate night-time vertical mixing strength likely reflects the rapid urbanization of industrialized eastern China.

Photolysis of oxygenated volatile organic compounds (OVOCs) produces a primary source of free radicals, including OH and inorganic and organic peroxyl radicals (HO_2 and RO_2), consequently increasing photochemical ozone production. The amplification of radical cycling through OVOC photolysis provides an important positive feedback mechanism to accelerate ozone production. This amplifier effect is most significant in regions with high nitrogen oxides (NO_X) and VOC concentrations such as Wangdu in China. Using a 1-D model with in-situ observations at Wangdu and the Master Chemical Mechanism, we find that ozone oxidation from RO_2 is comparable to HO_2 and that the condensed 3-D model mechanism severely underestimates the OVOC amplifier effect and the resulting enhancements in the production of peroxyl radicals and ozone. Current 3-D modeling assessments of surface and boundary oxidation capacity and ozone control strategies are therefore also biased, underestimating the effects of anthropogenic and biogenic VOCs in polluted regions.

Empirical fitting of high-resolution satellite composite data of nitrogen dioxide (NO_2) provides a valuable method for estimating city-scale NO_X emissions. However, the uncertainties, such as those from the satellite sampling process, have not been systematically assessed. After analyzing the method uncertainty with idealized city plume

data, we make use of the simulation results from a 4-km CMAQ model simulation of megacity clusters in the Yangtze River Delta (YRD) region and generate synthetic datasets through resampling using the orbits and pixels of the Ozone Monitoring Instrument (OMI) and the TROPOspheric Monitoring Instrument (TROPOMI). As such the emission properties of the datasets are known. We then apply the exponentially modified Gaussian (EMG) fitting method to estimate the emissions using the original 4-km NO_2 columns as well as the resampled NO_2 columns to understand the factors contributing to emission estimate uncertainties in this method. The analysis of idealized Gaussian city plumes shows the orientation dependence of the low bias in NO_X emission estimates due to the sampling bias of the coarse-resolution OMI pixels. This OMI sampling bias is reproduced using the synthetic dataset based on the 4-km CMAQ simulation. Based on the two city cases we studied, we suggest using a range of integral distance from 100 to 200 km and find the maximum NO_X emission estimate as the optimal value when the integral distance is not known. Overall, our analysis shows that the EMG fitting method can be applied to OMI and TROPOMI observations to examine city-scale emission trends, although factors such as the size of the city emission, the emission dependence on the cross-section integral distance, and background interference need to be investigated.

CHAPTER 1. INTRODUCTION

Ground-level ozone is a secondary atmospheric pollutant that damages human and vegetation health (U.S. EPA, 2013). The chemical production of ground-level ozone involves the photochemical reactions between nitrogen oxides (NO_X = NO + NO_2) and volatile organic compounds (VOCs) (Seinfeld et al., 2016). China is experiencing high levels of ozone due to high precursor emissions in association with rapid urbanization and industrialization in past decades (Wang et al., 2017; Zhao et al., 2013). In this fast-changing environment, a better understanding of the ozone formation process, as well as accurate estimations of the ground-level ozone and its precursors, are sorely needed for effective pollutant control measures.

In this thesis, I focus on extending the current knowledge of the relationship between ozone production and precursor emissions, using modeling simulations coupled with extensive in situ observations in China. In CHAPTER 2, I extend the current relationship between peak ozone concentration and precursor emissions to peak time and use the ozone measurements in China cities as constraints to diagnose the NO_X and VOC emissions as well as the nighttime mixing height. In CHAPTER 3, I use box and 1-D models to investigate the local radical activities in a small town in North China Plain based on observations from a field campaign and find that the current 3-D model with simplified mechanism underestimate the RO_2 production from the intermedia oxygenated volatile organic compounds (OVOCs), leading to an underestimation of the effects of VOCs and NO_X emissions on ozone production. In CHAPTER 4, I test the uncertainty of the current empirical fitting method of NO_X emissions from satellite observations, using both a

generated ideal plume and plumes from simulations. I find that the accuracy of the fitting method largely depends on the cross-section integral distance. The findings and future work perspectives will be organized in CHAPTER 5.

1.1 Ozone-precursor relationship

In the troposphere, over 90% of the ozone is due to chemical production globally (Hu et al., 2017; Young et al., 2013). The production of ozone involves the photolysis of the nitrogen dioxide (NO_2) that produces oxygen atoms (O) and nitrogen monoxide (NO). The oxygen atoms then react with oxygen molecules and produce ozone (O_3) (R1.1, R1.2). The NO can destruct O_3 by fast reactions, which is often referred to as the titration effect (R1.3).

$$NO_2 + h\nu \rightarrow NO + O \quad \text{(R1.1)}$$

$$O + O_2 \rightarrow O_3 \quad \text{(R1.2)}$$

$$NO + O_3 \rightarrow NO_2 + O_2 \quad \text{(R1.3)}$$

(R1.1-R1.3) form a null cycle that would not yield ozone. However, when the carbon monoxide (CO) or hydrocarbons (RH) exist in the atmosphere, they will react with the OH radical produced from the photolysis of O_3 and form peroxyl radicals (HO_2 or RO_2) through (R1.4-R1.7).

$$O_3 + h\nu \rightarrow O(^1D) \quad \text{(R1.4)}$$

$$O(^1D) + H_2O \rightarrow 2OH \quad \text{(R1.5)}$$

$$OH + CO + O_2 \rightarrow HO_2 + CO_2 \quad \text{(R1.6)}$$

$$OH + RH + O_2 \rightarrow RO_2 + H_2O \quad \text{(R1.7)}$$

The HO_2 and RO_2 can oxidize NO into NO_2, causing a net production of O_3 and forms oxygenated volatile organic compounds (OVOCs) (R1.8-R1.10). The OVOCs can react with OH in a way similar to the hydrocarbons, but they can also provide a secondary source of the peroxyl radicals through photolysis (R1.11, R1.12).

$$HO_2 + NO \rightarrow OH + NO_2 \quad \text{(R1.8)}$$

$$RO_2 + NO \rightarrow RO + NO_2 \quad \text{(R1.9)}$$

$$RO + O_2 \rightarrow R'CHO + HO_2 \quad \text{(R1.10)}$$

$$R'CHO + OH + O_2 \rightarrow R'C(O)O_2 + H_2O \quad \text{(R1.11)}$$

$$R'CHO + h\nu + 2O_2 \rightarrow R'O_2 + CO + HO_2 \quad \text{(R1.12)}$$

Although both NO_X and VOCs are ozone precursors, the relationship between the ozone concentration and the precursor emissions is highly non-linear due to the contradict character of NO_X in ozone production. A high level of NO_2 would exhaust OH radicals by (R1.13) and halt the oxidation of VOCs.

$$NO_2 + OH \rightarrow HNO_3 \quad \text{(R1.13)}$$

The relationship between ozone production and ozone precursor emissions has been well studied as it is an important factor in establishing effective ozone control strategies

(Blanchard et al., 2001; Geng et al., 2008; Jimenez et al., 2004; Parra et al., 2009; Ren et al., 2013; Zhao et al., 2009a). Under high VOC/NO_X emission ratios, the ozone is much more sensitive to NO_X emissions than VOC emissions, thus called a NO_X-limited regime. Increasing NO_X emissions will enhance ozone production dramatically, while increasing VOC emissions will yield a limited increase in the ozone production rate. Under low VOC/NO_X emission ratios, the ozone is more sensitive to VOC emissions than NO_X emissions, thus called a VOC-limited regime. Increasing VOC emissions will significantly enhance ozone production while increasing NO_X emissions will lower the ozone production rate. In between the above two regimes, ozone can be sensitive to both emissions and is often referred to as the transition regime. The ozone-precursor relationship can be critical for policymakers, for example, reducing NO_X emission will lead to an enhancement of ozone if the local emissions locate in the VOC-limited regime.

1.2 Ozone pollution in China

China has been experiencing aggravating air pollution problems due to high precursor emissions in association with rapid urbanization and industrialization (Duncan et al., 2016; Lin et al., 2013; Wang et al., 2017; Zhao et al., 2013). In 1996, China set the first ambient air quality standard, regulating ozone and other eight critical atmospheric pollutants. The particular matters (PM) are the most urgent air quality problems in China for decades (Ma et al., 2015; Xie et al., 2016), while the control policy of the PM also affects ozone concentration by regulating NO_X emissions. From 2013 to 2017, the emission of NO_X has decreased by 21%, and the MDA8 ozone concentrations increase by 10-20% during the same period under a stable VOC emission (Zheng et al., 2018; Ma et al., 2016).

The increasing summertime ozone levels in the cities raise concerns about possible health issues. From June to July 2005, the maximum hourly ozone levels in Beijing reached 286 ppbv, four times the EPA ozone standard of 70 ppbv, and in one-third of the days, the ozone level exceed 120 ppbv (Wang, T. et al., 2006). Before 2012, the ozone observations in China are sparsely measured and extensive measurements are necessary for the analysis of ozone pollution in China. In 2012, the China Ministry of Ecology and Environment revised the maximum daily 8-h average ozone (MDA8 O_3) to 160 μg m^{-3} (~75 ppbv) and started to build the China National Environmental Monitoring Center (CNEMC) network. In 2013, the network system reports hourly real-time data of six criteria pollutants (O_3, CO, NO_2, SO_2, $PM_{2.5}$, and PM_{10}) and air quality index (AQI) from 450 sites in 74 cities. In 2020, the network has expanded to >1600 sites in 366 cities.

The data from CNEMC revealed the severe ozone pollution problem during summertime in China. In July 2017, for example, in the 364 cities with available observations, 65% of the cities have MDA8 O_3 exceeds the air quality standard of ozone for at least one day, and in 5 of the cites, the MDA8 O_3 exceeds the standard for longer than 20 days. Figure 1.1 shows the monthly average of the MDA8 O_3 in July 2017. High levels of ozone spread over the country, especially in the North Central Plain (NCP) region, the Yangtze River Delta (YRD) region, and the Sichuan Basin. Researches have also found that from 2013 to 2017, the ozone has been increasing by 1-3 ppbv yr^{-1} in both urban and background regions in China (Gao et al., 2017; Li et al., 2016). The enhancement of ozone levels indicates a strong chemical nonlinearity impact that lower NO_X emissions can lead to higher ozone concentrations. Meteorology conditions and less active heterogeneous activities due to lower aerosol surface concentration may also contribute to the

enhancement of ozone (Lou et al., 2014; Ding et al., 2019). Control measurements for ozone are urgently needed, and a better understanding of the ozone production process is necessary.

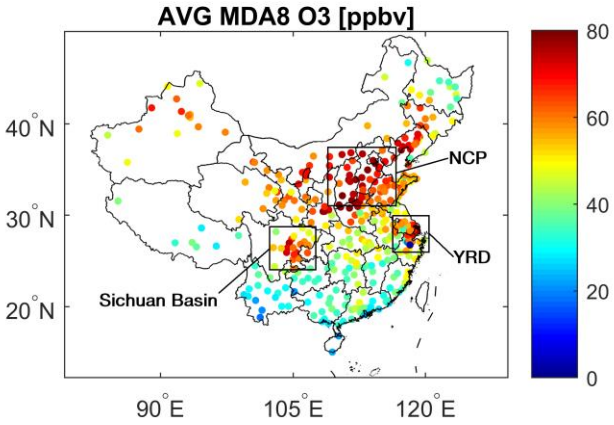

Figure 1.1 The monthly averaged maximum daily 8-h average (MDA8) ozone concentration in July 2017 over 364 cities in China

1.3 Chemical Transport Model

The Chemical Transport Models (CTMs) has been widely adopted to simulate the atmospheric photochemistry processes, to investigate the emissions and concentrations of air pollutants, and to determine the optimal pollutant control measure and predict the possible outcome. In this thesis, we adopted the Regional chEmical transport Model (REAM) for regional analysis, and we developed a box and a 1-D model for studies on local chemistry.

1.3.1 3-D REAM

The framework of the 3-D REAM is illustrated in Figure 1.2. The 3-D REAM has been widely used in studies over North America, East Asia, and other regions (Gu et al., 2014; Liu et al., 2012b, 2014; Wang, Y. et al., 2006, 2007; Xu et al., 2018; Zeng et al., 2006; Zhang et al., 2016; Zhang R. et al., 2017, 2018; Zhao et al., 2009b). The horizontal resolution of the model is 36 km with 30 vertical layers in the troposphere with timestep of 1 hour. Meteorological data are obtained from the Weather Research and Forecasting model (WRF 3.6) assimilations constrained by the National Centers for Environmental Prediction Climate Forecast System Version 2 (NCEP CFSv2) products (Saha et al., 2013). The initial and boundary conditions for chemical tracers are obtained from the GEOS-Chem model (v9-02) (Bey et al., 2001). The chemistry mechanism extends the GEOS-Chem chemistry mechanism with reactions involving aromatics, ethylene, and acetylene. The Multi-resolution Emission Inventory for China (MEIC) emissions for the year 2012 are adopted in the model for anthropogenic emissions of NO_X, VOCs, and CO (Zhang et al., 2009). The emissions are scaled by the diurnal ratio taken from the National Emissions Inventory (NEI), and there is no weekday-to-weekend variation. Biogenic emissions of isoprene are calculated using the Model of Emissions of Gases and Aerosols from Nature (MEGAN v2.1) (Guenther et al., 2012). Figure 1.3 shows the domain of the WRF and REAM model.

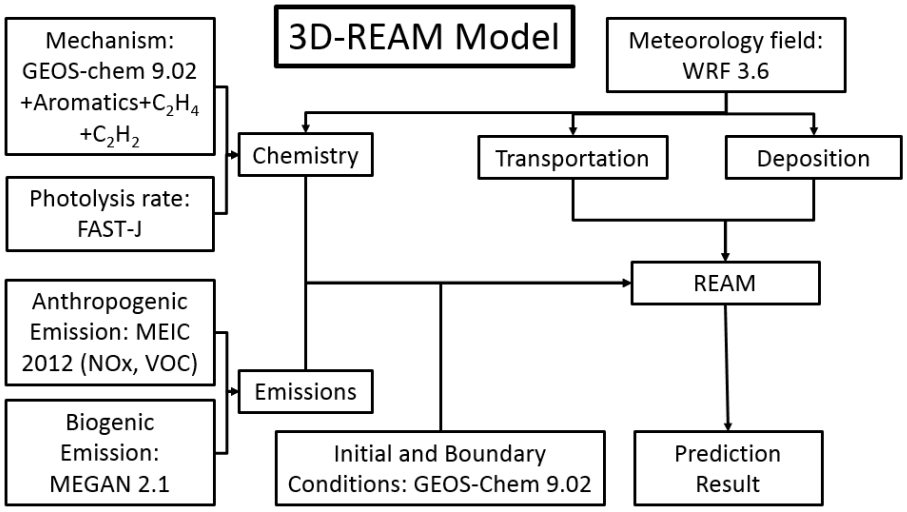

Figure 1.2 General structure of the 3-D REAM model

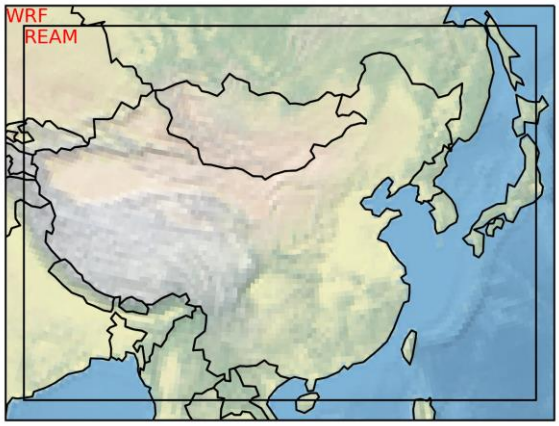

Figure 1.3 Domain of the WRF model and the REAM

1.3.2 Box and 1-D models

We developed a box model based on the chemical solver from REAM to simulate ozone with local chemistry. The time step of the box model is one minute. The box model is assembled with replaceable chemistry mechanisms. In this thesis, we adopt two mechanism: a simplified mechanism taken from REAM (i.e. the GEOS-Chem v9.02

mechanism with extends of aromatics, C_2H_4, and C_2H_2) and an explicit mechanism of the Master Chemical Mechanism (MCM 3.3.1) (Jenkin et al., 1997; Saunders et al., 2003; Jenkin et al., 2003; Bloss et al., 2005; Jenkin et al., 2012; Jenkin et al., 2015). We also extend the two mechanisms with chlorine related reactions, and the detailed description can be found in **Appendix A**. The NO_X and VOCs in the model can either use constraints from observations or specified by emission rates. The meteorology parameters, including temperature, pressure, water vapor concentrations, use the in situ observed values or simulation results from the WRF model if observations are not available. We assume that the box model represents the well-mixed boundary layer, so the height of the model and the boundary conditions use corresponding value simulated from 3-D REAM unless otherwise specified.

The 1-D model assembles a series of the box model vertically with the same vertical settings in 3-D REAM. The observed constraints are applied to the ground layer of the 1-D model. The meteorology parameters use the simulations from the WRF model and are constrained by the observations in the ground layer.

CHAPTER 2. OZONE-OBSERVATION DERIVED EMISSION AND NIGHTTIME MIXING CONSTRAINTS IN CHINA: DAYTIME PEAK TIME AND NIGHTTIME MIXING

2.1 Introduction

As we discussed in Chapter 1, the ground-level ozone is a secondary air pollutant that harms human and vegetation health, and high-level ozone frequently occurs in summer in large cities where power plants and vehicles emit large quantities of ozone precursors, i.e., NO_X and VOCs. Parra et al. (2009) and Blanchard et al. (2001) have found that in urban areas, due to heavy traffic, NO_X emissions often exceed VOC emissions by a large extent and locate in the VOC-limited regime. However, in China megacity clusters, ozone production is usually found in the transition regime, and the ozone production rate can be sensitive to both NO_X and VOC emissions (Jin et al., 2015; Li et al., 2013; Liu et al., 2012a; Ran et al., 2009; Xing et al., 2011).

The daily pattern of ozone concentration reflects the dynamic balance among chemical production and loss, deposition process, and transport processes (Zhang Y. et al., 2016; Bloomer et al., 2010). In the daytime, ozone reaches its daily peak due to photochemical production in the afternoon. At night, the ozone chemical production is negligible, and due to the titration effect by NO emissions in a stable nocturnal boundary layer in urban regions, ozone concentrations can be extremely low (Nolle et al., 2002; Simon et al., 2014).

A commonly used ozone-precursor relationship is the dependence of peak concentration of daytime ozone on NO_X and VOC emissions, which is also known as the empirical kinetic modeling approach (EKMA) diagram (e.g., Ashok et al., 2016; Kinosian et al., 1982; Tao et al., 2018). In this study, we extend the ozone-precursor relationship to ozone peak time and investigate the potential of using extensive ozone observations in China to improve observation constraints on model simulated ozone-precursor relationships (Li J. et al., 2019). We use the observations of ozone in July 2014 as an example to demonstrate this potential. We show that ozone peak time's dependence on NO_X and VOC emissions offers new constraints on the emissions that are different from those placed by the observed peak concentrations. Therefore, the discrepancies between simulated and observed ozone peak time and peak concentrations can be applied to understand the biases in ozone precursor emission inventories and provide pertinent guidance on adjusting model-based emission control strategies. We also investigate the reasons for a consistent low bias in model simulated nighttime ozone concentrations compared to the observations.

2.2 Data and Methods

2.2.1 The CNEMC network

As introduced in Chapter 1, CNEMC has established ambient atmosphere quality monitoring networks across the country since 2013, reporting hourly real-time data of six criteria pollutants (O_3, CO, NO_2, SO_2, $PM_{2.5}$, and PM_{10}) and air quality index (AQI) in cities online (http://www.cnemc.cn). Recent studies have been using the data for analyzing the current air quality issues (Li, K. et al., 2019; Liu, H. et al., 2018; Lu et al., 2018). In

this work, we analyzed the hourly surface ozone observations from 861 sites in 189 cities for July 2014. For each site, we remove all the data that are higher than 4 times the monthly average of 3-hour running mean data for the hour of the observations. We then group the data by the hour of the observation and apply Tukey's fences to remove outliers. Specifically, we remove the outlier data which are outside the range of Q_1-k(Q_3-Q_1) and Q_3+k(Q_3-Q_1), where Q_1 and Q_3 are the 25th and 75th quartiles, respectively, and k=1.5 (Tukey, 1993). A total of 2.3 % of the measurement data are removed. We compute the city averages based on the observations at all sites in a city. The peak time of ozone is converted to local sun time base on the longitude of the city.

2.2.2 The 3-D REAM model

In this study, we use the 3-D REAM model to analyze the regional distribution of the ozone and the sensitivity of ozone peak concentration and peak time to NO_X and VOC emissions. The detailed description of the 3-D REAM model is in Chapter 1. We run the model for July 2014, the same period as the data we used. The model is spun up for 10 days for initialization.

The box model is also used for simulating the ozone peak concentration and peak time under a broad range of NO_X and VOC emissions. The meteorological, physical, and chemical parameters including temperature, pressure, water concentration, boundary layer height, photolysis rates, deposition rates, and aerosol surface area are averaged hourly for city grid cells with surface ozone observations. Advection transport is specified with a lifetime of 5.3 hours, corresponding to an average city scale of 100 km and an average wind speed of 5.2 m s^{-1}. Hourly background concentrations for ozone are set at the 5th

percentile value of the observations. Each simulation is run until a steady-state when the differences in ozone peak concentration and time converge to a difference of < 1 % from the previous day. A total of 400 simulations were conducted for NO_X emissions ranging from 0-4.5×10^{16} molecules m^{-2} s^{-1} and VOC emissions ranging from 0-1.4×10^{17} molecule m^{-2} s^{-1} by carbon. The upper limits of NO_X and VOC emissions correspond to 3 times of average MEIC emissions for the cities with surface ozone observations.

2.3 Results

2.3.1 Correlations of O3 Peak Concentration and Time to NO_X and VOC Emissions

The ozone-precursor relationships to be studied can be simply illustrated by the correspondence of ozone peak time and concentration to NO_X and VOC emissions in China. Figure 2.1a and Figure 2.1b show the correlations between ozone peak concentration and NO_X and VOC emissions, respectively. The correlation coefficients of ozone peak concentration with NO_X and VOC emissions are comparable at 0.54 and 0.53, respectively. In small cities with NO_X emissions <1×10^{15} molecules m^{-2} s^{-1}, the transport processes dominate the concentrations of ozone and its precursors, and we remove these four sites (3 %) to focus on the effects of local ozone photochemistry. Figure 2.1c shows that the observed ozone peak time highly correlates with MEIC NO_X emission (R = 0.75) in the cities with strong NO_X emissions (>1×10^{15} molecules m^{-2} s^{-1}). The ozone peak time delays from 1-2 pm to 5-6 pm as the NO_X emissions increase from 1×10^{15} molecules m^{-2} s^{-1} to 1×10^{17} molecules m^{-2} s^{-1}. The ozone peak time is also correlated with VOC emission with an R-value of 0.56 (Figure 2.1d). Figure 2.1 implies that the EKMA-type relationship

between ozone peak concentration and its precursor emissions may be extended to ozone peak concentration in China.

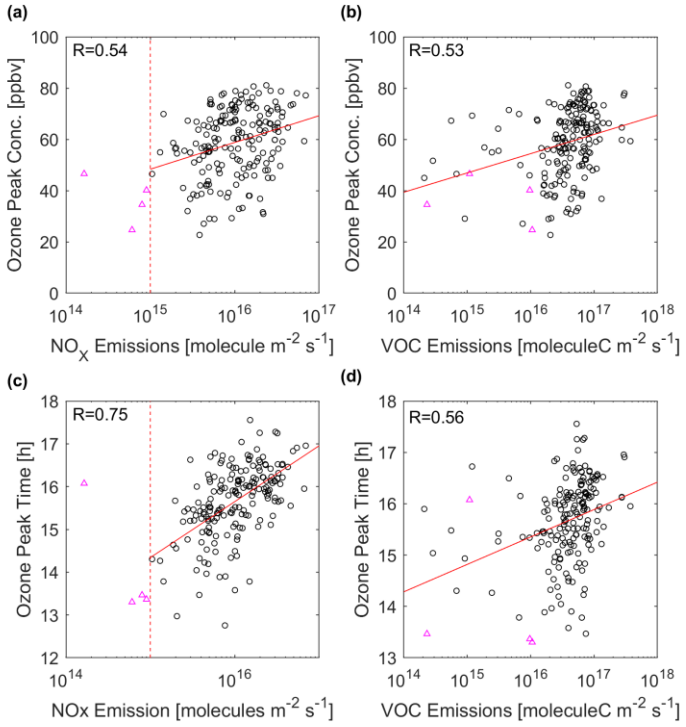

Figure 2.1 Observed ozone peak concentration and time as a function of NOx and VOC emissions in the MEIC inventory, respectively, for July 2014. The pink triangles denote urban regions with NOx emissions < 10^{15} molecules m^{-2} s^{-1}, which are excluded from this study. The red line is a least-squares regression for urban regions with NOx emissions > 10^{15} molecules m^{-2} s^{-1}.

2.3.2 Modeling Analysis of the Observations

The observed and simulated distribution of maximum daily 8-h average (MDA8) ozone concentrations in the cities are evaluated in Figure 2.2a. The mean simulated ozone concentration over the city grid cells is 57 ± 12 ppbv, which is comparable to the observed 53 ± 13 ppbv, with an overall correlation coefficient of 0.72. To understand regional characteristics, we grouped the data into six regions by economic development and

topography (Figure 2.2b): North Central Plain (NCP), Northeast (NE) region, Yangtze River Delta (YRD), Northwest (NW) region, Southwest (SW) region, and Pearl River Delta (PRD). Table 2.1 summarizes the regional statistics. The observed mean MDA8 ozone concentrations range from 41 to 64 ppbv in the six regions. The highest mean ozone concentration occurs in the NCP region, and the lowest mean concentration occurs in the PRD region. The model results differ from the observations by 0-13 ppbv in the six regions and the correlation coefficients between observed and simulated ozone range from 0.61 to 0.81.

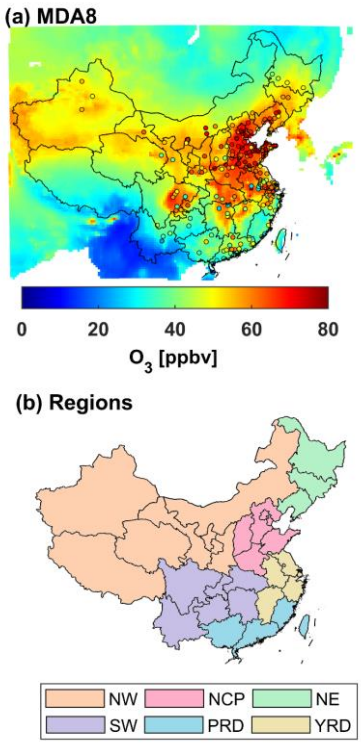

Figure 2.2 Panel (a) shows the simulated (background) and observed (circle) maximum daily 8-h average ozone (MDA8 O_3) concentrations for July 2014. Panel (b) shows the 6 regions: Northwest ("NW", orange), North China Plain ("NCP", red), Northeast ("NE", green), Southwest ("SW", purple), Pearl River Delta ("PRD", blue), and Yangtze River Delta ("YRD", yellow).

Table 2.1 Statistics of observed and simulated means and standard deviations (ppbv) of MDA8 ozone in 6 regions for July 2014.

	NCP	NE	NW	PRD	YRD	SW	Overall
Observations	64±9	56±9	55±11	41±11	52±8	43±12	53±13
Simulations	64±8	59±9	55±6	42±6	58±12	56±14	57±12
Correlation coefficient	0.61	0.78	0.72	0.81	0.62	0.67	0.72

To further investigate the relationships of ozone peak concentration and time with NO_X and VOC emissions, we conduct two series of sensitivity tests: (1) NO_X emissions changing from -50 % to +50 % with an increment of 10 %, and (2) VOC emissions changing from -50 % to +50 % with an increment of 10 %. Figure 2.3 shows the monthly mean results of the sensitivity simulations in comparison with the observations. VOC emissions enhance the ozone peak concentration nearly linearly, while the NO_X emissions affect the ozone peak concentration differently. In the NW and SW regions, the ozone peak concentration increases with NO_X emissions, but the sensitivity decreases with increasing NO_X emissions. The peak ozone and NO_X emission relationship is no longer monotonic in the other four regions. While increasing NO_X emissions decrease the ozone peaks, decreasing NO_X emissions eventually also decrease the ozone peaks, but the turnover points are shifted to the left in the NCP, YRD, and NE regions. The sensitivity results of the ozone concentration to the emissions agree with previous studies (Li et al., 2013; Xing et al., 2011).

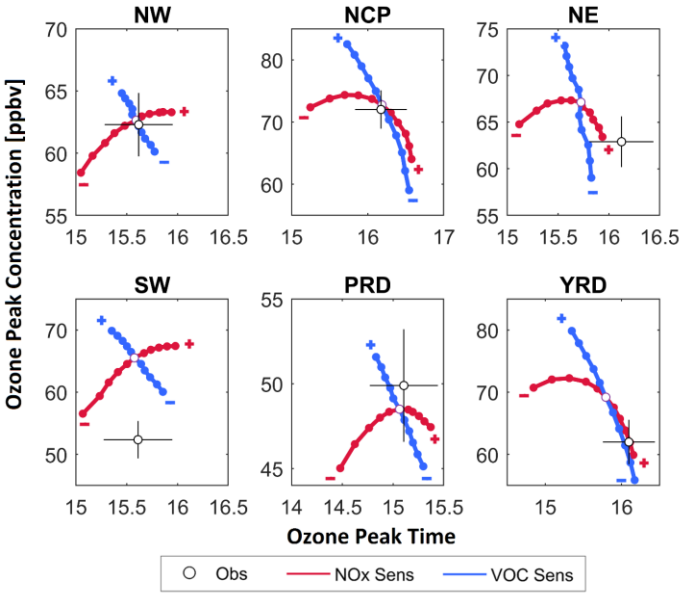

Figure 2.3 Sensitivities of ozone daily peak concentration and peak time to VOCs and NO_X emissions in the 6 regions for July 2014. The black open circles and lines show the observed peak averages and the corresponding standard deviations. The open circles at the intersection of the red and blue lines denote the standard simulation results. The red lines with solid dots show the sensitivities to NO_X emissions ("NO_X Sens"); the blue lines with solid dots show the sensitivities of VOC emissions ("VOC Sens"). (+) and (-) denote increase and decrease of emission in the model, and each dot denotes an increment or decrement of 10% in emissions. Sensitivities up to plus or minus 50 % are shown.

In contrast to the complex ozone peak concentration sensitivities to NO_X emissions, the sensitivities of ozone peak time to NO_X and VOC are monotonic. Increasing NO_X emissions delays the ozone peak time while increasing VOC emissions advances the ozone peak time in all 6 regions. For the same 50% change of emissions, the effect of NO_X is larger than VOCs, which partly explains the higher correlation coefficient between ozone peak time and NO_X emissions than those between ozone peak time and VOC emissions or for ozone peak concentration.

The monotonic sensitivities of ozone peak time to NO_X and VOC emissions compared to the more complex response of ozone peak concentration to emissions imply that the observations of ozone peak time provide good constraints on model simulations other than the observations of ozone peak concentration. It is only because the ambient ozone standard is based on concentrations that the observations of ozone peak time are usually not applied to evaluate model simulations. A further useful property of the simulated ozone peak time is that the impact of changing NO_X and VOC emissions concurrently by 50 % are nearly additive (Figure 2.4): the change of ozone peak time in a simulation of changing NO_X and VOC emissions by 50 % concurrently is close to the sum of the simulated changes of changing NO_X or VOC emissions by 50 % alone. This additive effect does not exist in the ozone peak concentration simulations due to chemical nonlinearity (Figure 2.5), suggesting that the observed and simulated sensitivities of ozone peak time are easier to interpret than ozone peak concentration in urban regions of China.

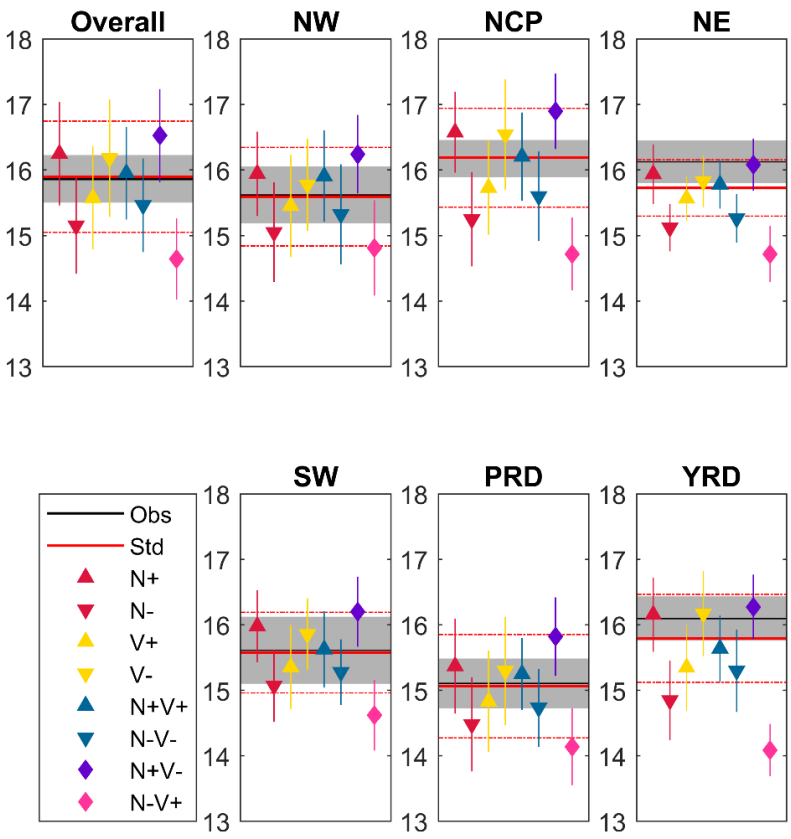

Figure 2.4 The sensitivities of simulated ozone peak time to NOx and VOC emissions for July 2014. N+: increase NOx emissions by 50%, N-: decrease NOx emissions by 50%, V+: increase VOC emissions by 50%, V-: decrease VOC emissions by 50%, N+V+: increase both NOx and VOC emissions by 50%, N-V-: decrease both NOx and VOC emissions by 50%, N+V-: increase NOx emissions by 50% and decrease VOC emissions by 50%, N-V+: decrease NOx emissions by 50% and increase VOC emissions by 50%

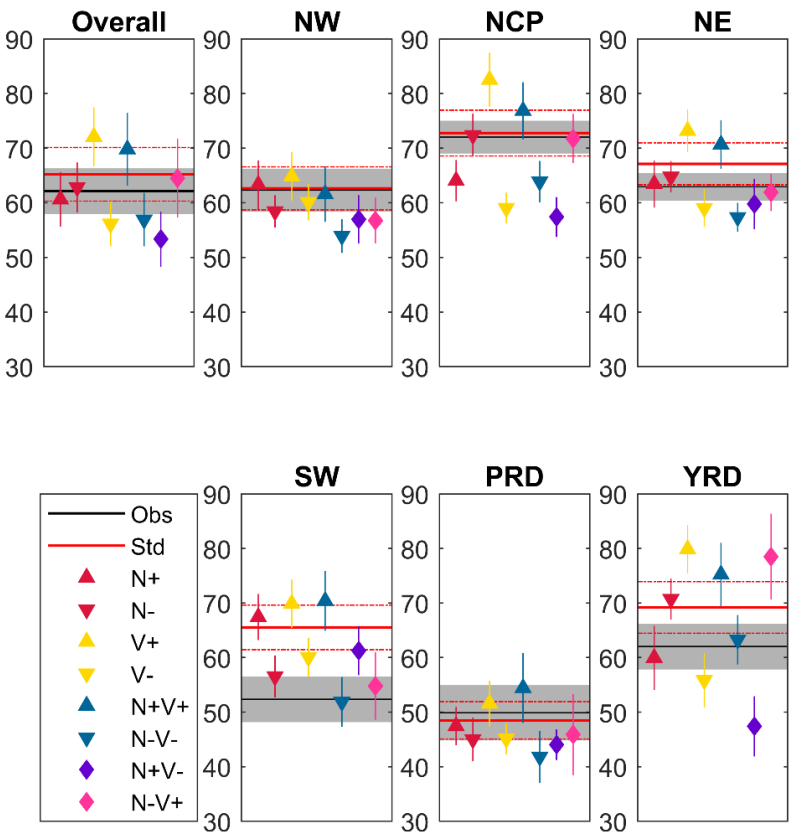

Figure 2.5 Same as Figure 2.4 but for ozone peak concentration

We examine in more detailed chemical processes leading to these sensitivity results. The chemical production of ozone is due to the oxidation of NO by the hydroperoxy (HO_2) radicals or organic peroxy (RO_2) radicals. Peroxy radicals are mostly produced from the reactions of VOCs with OH. Photolysis of oxygenated VOCs (OVOCs) is also a large primary source of peroxy radicals in polluted urban regions. The reaction of OH with NO_2 is a large sink of radicals and NO_X (Liu et al., 2012a). The sensitivities of OH, HO_2+RO_2, NO_X, and the rates of OVOC photolysis, the reaction rate of OH and NO_2, and chemical

production rate of O_3 (pO_3) to 50% changes of NO_X or VOCs are shown in Figure 2.6. The sensitivity results show that NO_X and VOC emissions affect ozone peak concentration and peak time in different ways. A 50% increase of NO_X emissions increases the radical sink through the reaction of OH and NO_2, suppressing radical concentrations. The net effect is a decrease in ozone production and peak ozone concentration. A 50% decrease of NO_X emissions has the opposite consequence. The radical suppressing effect by an increase of NO_X is larger in the early morning when the primary radical source is smaller than at noon. As a result, the ramping up of ozone production is delayed, and the ozone peak time is later. A 50% increase of VOC emissions increases HO_2 and RO_2 concentrations but does not affect NO_X concentrations as much, thereby increasing ozone production and peak concentrations. The effect of VOC emissions on ozone peak time is largely due to the photolysis of OVOCs, which peaks at noon, while ozone peak time is in mid-afternoon (Figure 2.3). A 50% increase of VOC emissions increases OVOC photolysis, shifting HO_2 and RO_2 concentration peak towards noon and making ozone peak time occur in earlier afternoon. Similarly, a 50% decrease of VOC emissions delays ozone peak time.

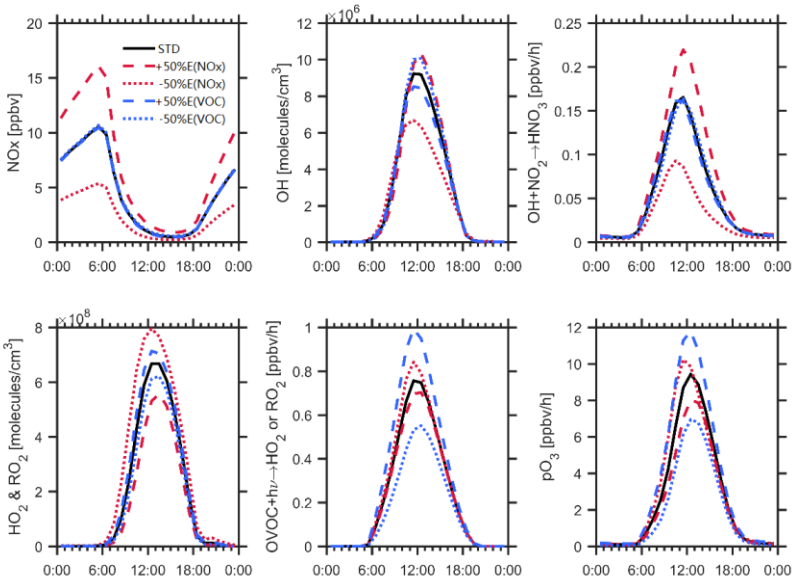

Figure 2.6 Sensitivities of OH, HO_2+RO_2, NO_X, and the rates of OVOC photolysis, the reaction rate of OH and NO_2, and pO_3 to 50 % changes of NO_X or VOCs at urban sites in this study for July 2014. The black lines are the results from the standard model; the red dashed lines show the results from a 50 % increase of NO_X emissions; the red dotted lines show the results from a 50 % decrease of NO_X emissions; the blue dashed lines show the results from a 50 % increase of VOCs emissions; the blue dotted lines show the results from a 50 % decrease of VOCs emissions.

2.3.3 Isopleth Diagram for Ozone Peak Time

The EKMA isopleth diagram for the sensitivity of ozone to NO_X and VOC emissions has been widely used (Ashok et al., 2016; Kinosian et al., 1982; Tan et al., 2018). We use the 0-D box model to compute the EKMA-type diagrams for ozone peak concentration and time for the urban regions of China in this study. Averaged hourly regional transport time, deposition rates, background concentrations, wind speed, and boundary layer height are included to simulate the effect of advection, mixing, and

deposition. The results provide qualitative guidance on understanding the 3-D model results discussed previously.

Figure 2.7 shows the sensitivity diagrams. The peak ozone sensitivity diagram is as expected. Under high NO_X and low VOC emissions, peak ozone concentration increases with increasing VOC and decreasing NO_X emissions, although the VOC sensitivity is much higher than NO_X. Hence it is often referred to as the VOC-limited regime. Under low NO_X and high VOC emissions, which is often referred to as the NO_X-limited regime, peak ozone concentration increases with increasing NO_X emissions rapidly but is insensitive to VOC emissions. In the transition regime (near the NO_X to VOCs (N:C) emission ratio of 1:3 in Figure 2.7), peak ozone concentration increases with increasing NO_X or VOC emissions. If the N:C emission ratio increases (to the lower right of the N:C ratio of 1:3), the sensitivity of peak ozone concentration to VOC emissions increases while the sensitivity of peak ozone concentration to NO_X emissions turns from positive to negative.

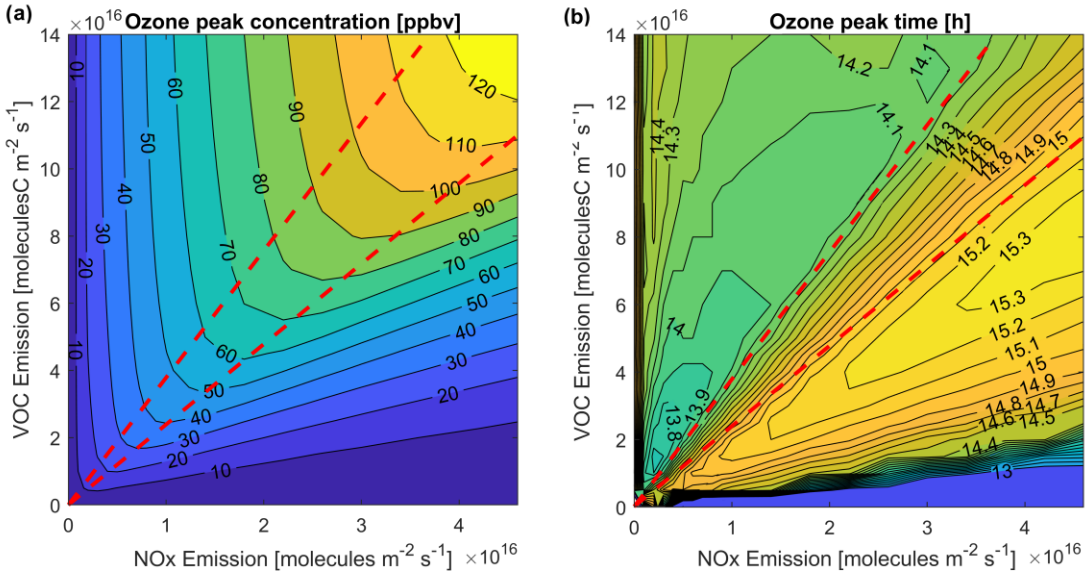

Figure 2.7 EKMA-type diagrams for the sensitivities of ozone peak concentration and time reacting to NO_X and VOC emissions simulated in the box model. The

range of NO_X and VOC emission increments covers up to 3 times of average urban emissions in model grid cells with urban surface ozone observations

On average, the urban regions in China fall into the transition regime: the behaviors of the ozone peak concentrations in the NW and SW regions are centered in the transition regime while the other regions lean towards the side of the transition regime with higher NO_X to VOC (N:C) emission ratios. Figure 2.7 shows that the sensitivity of ozone peak time in the vicinity of the transition regime is quite consistent. Increasing NO_X emissions or decreasing VOC emissions delays ozone peak time, in qualitative agreement with 3-D model simulation results. The reasons can be understood in Figure 2.6. For polluted urban regions, increasing NO_X emissions or decreasing VOC emissions has a similar effect of shifting the peak of peroxy radicals towards the afternoon and resulting in a later peak time of ozone. The former is due to an increase of the primary radical loss through the reaction of OH and NO_2, and the latter is due to a decrease of the primary radical source through the photolysis of OVOCs. As the N:C emission ratio continues increasing to be > 1:2 (lower right), ozone peak time is moved earlier by increasing NO_X emissions as peak ozone concentration decreases, while it is delayed by increasing VOC emissions as peak ozone concentration increases. In this regime, OH, ozone production, and chemical reactivity become increasingly suppressed by the reaction of OH and NO_2. Increasing VOC emissions decreases the effect of the reaction of OH and NO_2 since the fraction of OH reacts with VOCs would increase, and decreasing NO_X has a similar effect. When the N:C emission ratio continues to decrease from the 1:3 line (upper left), ozone peak time becomes less sensitive to NO_X and VOC emission. In the highly enriched VOC emission

regime, the peroxy radicals are not as sensitive to NO_X emissions as in the transition or high NO_X regime.

2.3.4 Diagnosing Potential Regional Emission Biases

The extended ozone-precursor relationships of Figure 2.7 can be applied to understand the implications of the observed changes in ozone peak time and concentration. For example, we would expect to see corresponding changes when urban emissions of NO_X or VOCs in a region decrease due to air quality control measures. The qualitative diagrams of Figure 2.7 provide quick guidance on the effectiveness of the control measures, and quantitative assessments can be carried out with modeling results (Figure 2.3). Here we illustrate the use of Figure 2.3 to understand potential problems in the emissions NO_X or VOCs in the model. More detailed analysis is recommended particularly with respect to more thoroughly understanding the model uncertainties. Figure 2.3 shows that the simulation results are very close to the observations for the NW and NCP regions, implying good emission estimation, consistent with previous studies (Guo et al., 2019; Li et al., 2018). For the NE region, the model overestimates the observed ozone peak value and an early ozone peak time. To correct for both biases, the best solution is to increase NO_X by 50%. For the SW region, the ozone peak time is well simulated, but the ozone peak concentration is overestimated. The former dictates that a decrease of NO_X emissions must be accompanied by a decrease of VOC emissions since decreasing one alone would lead to a bias in simulated ozone peak time and reducing both emissions is optimal (Figure 2.5). Previous research suggested that MEIC may overestimate VOC emissions for 67% in Sichuan province in the SW region, consistent with our results (Zhou et al., 2019). For the PRD region, the model-observation difference is within the variability of the observed data.

For the YRD region, the model estimates a higher peak concentration and an earlier peak time than the observations. These biases can be corrected by either increasing NO_X emissions or reducing VOC emissions. Since previous studies found overestimations of NO_X emission (Kong et al., 2019; Wu et al., 2017; Zhang L. et al., 2018; Zhao et al., 2018), the simulation results of Figure 2.3 indicate that VOC emissions are also overestimated. The potential biases in the emissions discussed here need other methods such as direct measurements of NO_X and VOC concentrations or emissions to corroborate.

2.3.5 Uncertainty

For urban regions of China, Figure 2.7 qualitatively explains the additional information obtained by extending the ozone-precursor relationships from peak concentration to peak time. In and around the transition regime, ozone peak time is sensitive to both NO_X and VOC emissions, and its sensitivity to NO_X emissions is much more straightforward than that of peak ozone concentration. There are uncertainties of using the ozone-precursor relationships, which apply for the previously established ozone peak concentration as well as ozone peak time discussed here. One caveat is that the observations of ozone are reported every hour. When comparing model results to the observations, hourly data are also used. Assuming that the precision error follows a Gaussian distribution with a 95th percentile range of 1 h. For N observations, the uncertainty is therefore $0.25/\sqrt{N}$ h. For a city, one-month data have a precision uncertainty of 0.045 h. Since we considered regional data and the number of cities for each region is >16, the precision uncertainty of ozone peak hour is <0.011 hr, which is negligible compared to the standard deviations. The precision of ozone peak time and concentration can be improved by increasing the observation frequency from every hour to every 10 min,

which can be easily achieved with today's technology. The same frequency must also be used for model data.

There are other factors to be considered which introduce uncertainties. The standard deviation of the observed regional ozone peak concentrations is ~3 ppbv, similar to previous studies for longer periods (Li K. et al., 2019; Lu et al., 2019). The model simulated ozone systematic uncertainties are difficult to assess due in part to nonlinear chemistry (Liu et al., 2012a). Previous studies mostly focused on ozone peak concentrations. In Mexico City, diurnal patterns of NO_X and VOC emissions can affect ozone peak concentrations by up to 17 % (Ying et al., 2009). If we remove the diurnal variations of NO_X and VOC emissions, the largest effects occur in the NCP, NE, and PRD, where ozone peak time is delayed by ~0.25 h, and ozone peak concentration decreases by 0.5 and 1 ppbv in NCP and YRD regions, respectively (Figure 2.8). The dry deposition also affects surface ozone (Zhao et al., 2019). Increasing or decreasing dry deposition rate by 10% does not affect simulated ozone peak time but changes ozone peak concentrations by up to 2 ppbv (Figure 2.9). Meteorology factors can also influence ozone concentrations (Hu et al., 2010; Lin et al., 2008), and dedicated studies are required. In general, the regional and monthly averages used in this study are less sensitive to meteorological biases than considering a single city.

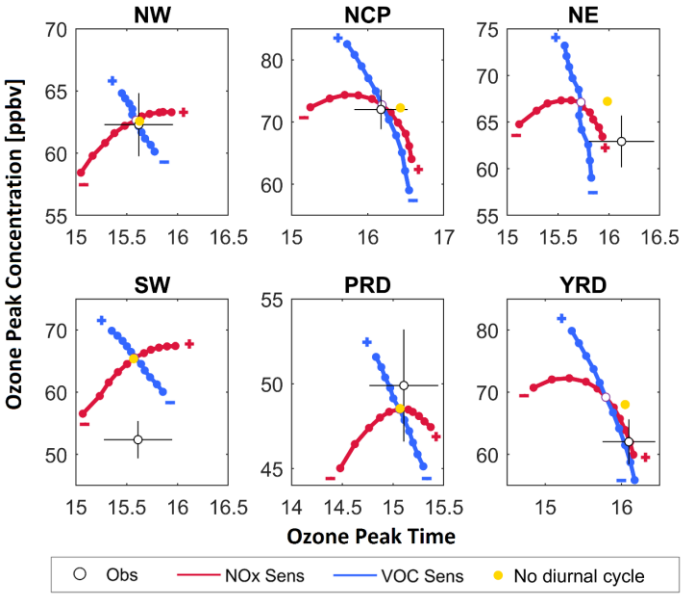

Figure 2.8 Same as Figure 2.3 with and extra case for removing the diurnal cycle of the emissions, marked as yellow dot.

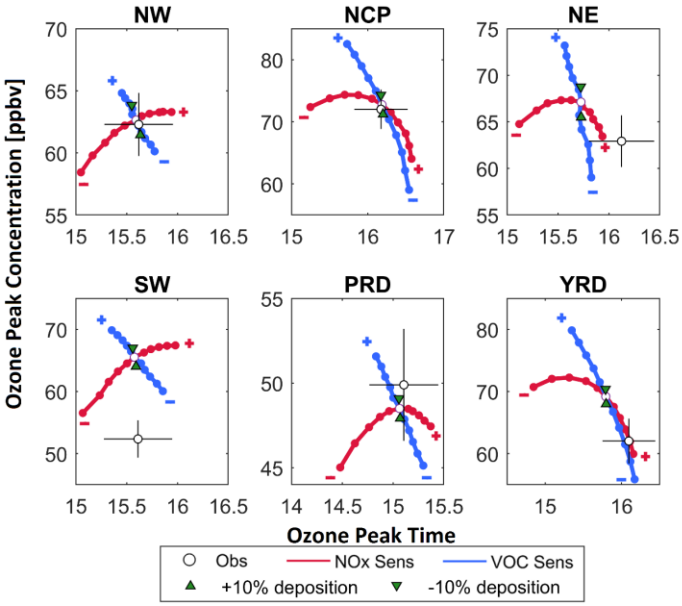

Figure 2.9 Same as Figure 2.3 with two extra cases for 10% enhancement and 10% reduction of the dry deposition rate of ozone, marked as green triangular pointing upward and downward separately.

2.3.6 Nighttime mixing

Figure 2.10 compares the monthly mean of the nighttime ozone concentration (8 PM to 8 AM) at urban sites from observation and simulation. The simulated nighttime ozone concentrations never exceed the observed level, and the difference between simulated and observed nighttime ozone concentrations can be as much as 50 ppbv. High nocturnal ozone concentrations were also observed elsewhere over the United States and other regions, and they were attributed to specific regional circulation systems including low-level jet (LLJ), land-sea breeze, down-valley wind, or typhoon (Corsmeier et al., 1997; Hu et al., 2013; Reitebuch et al., 2000; Kulkarni et al., 2013; Eliasson et al., 2003; Salmond et al., 2002; Jiang et al., 2015). However, they cannot explain the model low biases of simulated nocturnal ozone in every urban region across China.

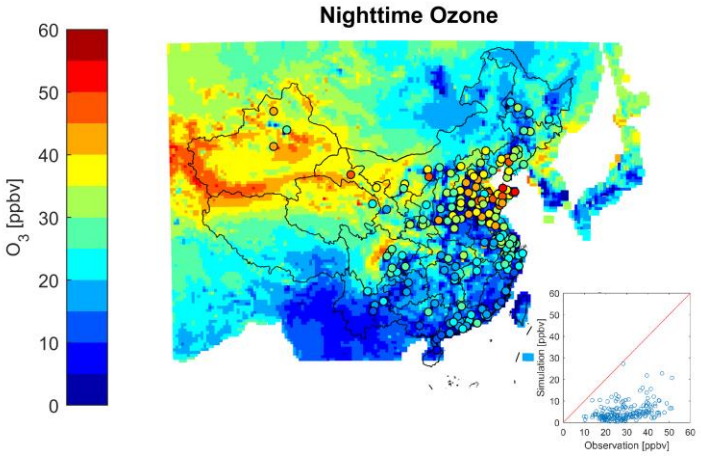

Figure 2.10 The distribution of simulated nighttime ozone in China and the observed nighttime ozone in the cities. The simulated ozone concentration from the corresponding grids of the cities is compared to the observation. The red line corresponds to 1:1.

The nighttime chemical loss of ozone in urban regions is mostly due to the titration effect of NO. Therefore, the underestimation of nighttime ozone by the model may result from overestimated NO emission at night. We conduct three simulations with modified

NO_X emissions with the NO_X emissions reduced by 20%, 50%, and 80%, respectively, at night from 8 PM to 8 AM local time. The amount of reduced NO_X emission is moved to daytime from 8 AM to 8 PM local time to maintain the total NO_X emission. The results show that even when nighttime NO_X emissions are reduced by 80%, the model still cannot reproduce the observations in most regions except for the NW (Figure 2.11).

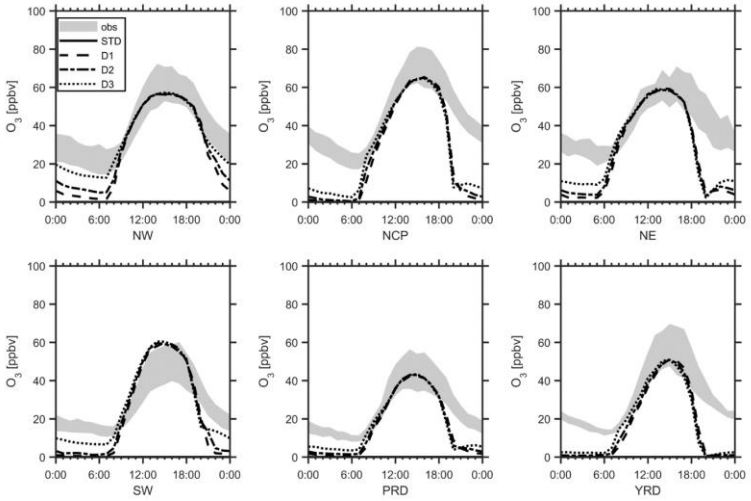

Figure 2.11 Simulated and observed diurnal variation of ozone concentrations in 6 regions. D1: 20% of NOx emissions at night from 8 PM to 8 AM to daytime; D2: same as D1, but the fraction is 50%; D3: same as D1, but the fraction is 80%.

Carslaw et al. (2005) find that the NO_2 can account for up to 17% of the total NO_X emissions from vehicle emissions, indicating a possible overestimating of the NO emissions from NO_X emissions. We conduct three sensitivity tests by changing the NO/NO_X emission ratio in the standard model to 20%, 50%, and 80%, respectively. The results show that the simulated nighttime ozone concentrations are still lower than the observations even with 80% of the NO_X emitted as NO_2 in most regions except for the NW and SW (Figure 2.12). In addition, Figure 2.10 shows that the model simulated low ozone

at night is regional in nature, so the horizontal advection is not the source of elevated nighttime ozone.

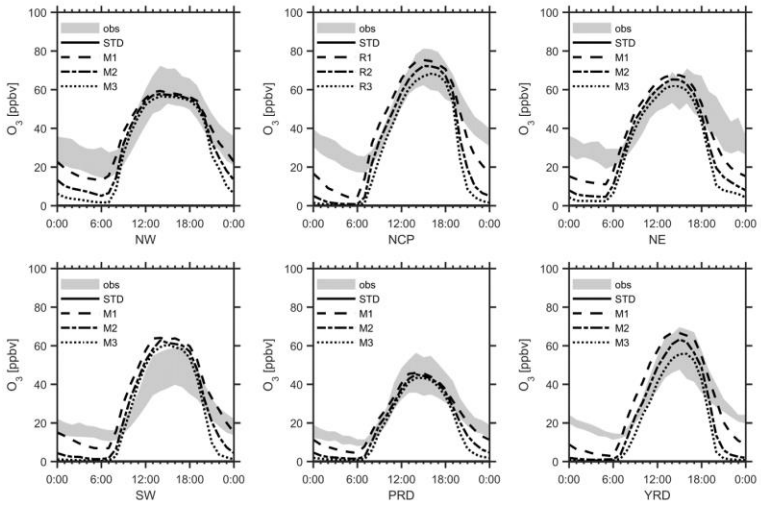

Figure 2.12 Simulated and observed diurnal variation of ozone concentrations in 6 regions. M1: 20% of NO_X emission is emitted as NO; M2: 50% of NO_X emission is emitted as NO; M3: 80% of NO_X emission is emitted as NO.

Another potential source of ozone at night is vertical mixing, which brings ozone from the residual boundary layer (RBL) downwards to the surface (Lin et al., 2008, 2010; Stock et al., 2014). Nighttime zone concentrations in the RBL are high due to daytime photochemical production. The observations of the nocturnal boundary layer height in China indicate a mixed layer from the surface to 200-500 meters (Wang, W. et al., 2016; Tang et al., 2016; Ma et al., 2013; Huang et al., 2017). In our model, the WRF simulation shows a very shallow nocturnal boundary layer of <200 meters, severely reducing the mixing of surface ozone with the RBL at night. We conduct three sensitivity tests, in which we enhance the nighttime (8 PM to 8 AM) vertical mixing from the surface to 100 meters, 200 meters and 500 meters, respectively. Figure 2.13 shows the model simulation results

in comparison to the observations. Enhanced vertical mixing at night significantly improves model simulation results. Accounting for the model bias, mixing to 200m is necessary for the model. Model simulated nighttime ozone is least sensitive to mixing height in PRD and YRD due in part to the advection of marine air masses from the southeast. The reasons for large underestimates of mixing height in urban regions by WRF are not understood and require further studies. The much more extensive urban landscape development in China than in the U.S. in recent years is likely a significant factor (Ching et al., 2018).

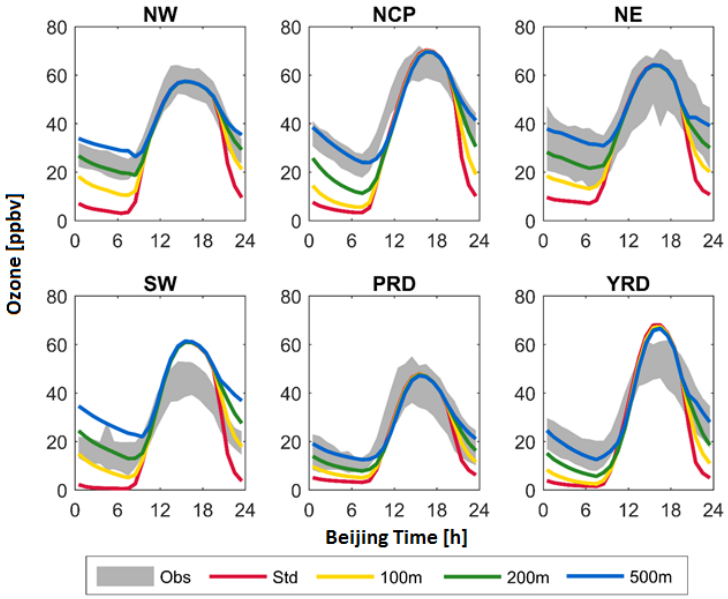

Figure 2.13 Observed and simulated ozone diurnal variations in 6 regions in Beijing Time. Gray shaded areas show the ozone observations within one standard deviation ("Obs"). The model results are shown in solid-colored lines for the standard simulation ("Std") and enhanced nocturnal mixing from 8 PM to 8 AM height to 100 meters ("100m"), 200 meters ("200m"), and 500 meters ("500m"), respectively.

2.4 Conclusion

In this study, we extend the ozone-precursor relationship to ozone peak time. The initial clue is simply based on the correlations of the observed ozone peak time and concentrations with NO_X and VOC emissions. We used the observations for the period of July 2014 to show that ozone peak time has better or comparable correlations with ozone precursor emissions in comparison to ozone peak concentration. It implies that the widely used EKMA diagram can be extended to observed ozone peak time and provides additional and independent constraints on ozone control strategies on the basis of widely available regulatory air quality monitoring data. We analyzed the observations for China, but the extended ozone-precursor relationships can be applied in other polluted regions.

We apply the 3-D REAM model with an extensive suite of sensitivity simulations to examine the sensitivities of ozone peak time and concentrations to NO_X and VOC emissions. The 3-D model sensitivity results are corroborated with the emission sensitivity isopleth diagram for ozone peak time similar to the EKMA diagram for ozone concentrations. The sensitivity distributions of ozone peak time and concentration differ significantly, indicating that the sensitivities of ozone peak time and concentration are complimentary for regions with large anthropogenic emissions such as China.

Since ozone is a secondary pollutant produced from photochemical reactions, the near-surface observations are not affected as much by heterogeneously distributed emission sources as NO_X and VOCs. The longer chemical lifetime of ozone than NO_X and fast-reacting VOCs also makes its measurements more representative than its precursors. Furthermore, the measurements of ozone are more reliable and readily available than NO_X and VOCs in China and other regions. The extended ozone-precursor relationships developed here provide both qualitative and quantitative constraints on understanding the

effects on ozone by emission changes of NO_X and VOC. They can also be applied with air quality models to assess potential biases of NO_X and VOC emission inventories. In this work, we find that the emissions of ozone precursors are consistent with the observed ozone peak time and concentrations for the NW and NCP regions. In the NE region, NO_X emissions may have a low bias of 50%. In the SW region, both the NO_X and the VOC emissions are overestimated. In the YRD region, the VOC emissions are overestimated. In the PRD region, model results are in agreement with the observations within the uncertainties of the measurements. Such observation constraints on the basis of regulatory ozone observations can complement nicely the other measurement and modeling analysis methods for evaluating NO_X and the VOC emission inventories.

The uncertainties of the method developed here are similar to previous studies using the EKMA diagram (Moore et al., 2001; Tan et al., 2018). We examine specifically the uncertainties related to the diurnal variation of emissions and ozone dry deposition, and we find that they do not significantly affect the inference results of potential emission biases based on ozone observations. While not explicitly studied, the inference results are insensitive to short-term meteorology biases because the modeling analysis (e.g., Figs. 3-9) is based on monthly and regional averaged results. Depending on the applications of the extended EKMA diagram analysis, further uncertainty analysis needs to be carried out. Furthermore, we suggest that the ozone peak time sensitivity as we discussed here to be used as a model evaluation measure before the EKMA diagram is applied to understand the effectiveness of emission control on ozone concentrations.

We also find that the model greatly underestimates ozone concentrations at night. The regional pattern of the underestimation indicates horizontal transport cannot lead to

the underestimation, and chemical approaches by reducing NO emission at night without affecting daytime ozone concentrations have been failed for both moving NO_X emissions from nighttime to daytime and changing the NO_2/NO_X emission ratios. Underestimated vertical transport strength at night is the best possible explanation for the low surface ozone level in the model and observations indicate a mixing height of 100-500 meters is necessary.

CHAPTER 3. SECONDARY PRODUCTION OF OVOCS IN THE BOUNDARY LAYER STRONGLY ENHANCES OXIDATION CHEMISTRY AND OZONE PRODUCTION NEAR THE SURFACE

3.1 Introduction

Recent researches have revealed that oxygenated volatile organic compounds (OVOCs) are omnipresent in the atmosphere and strongly affect atmospheric oxidation (Shim et al., 2007; Yang et al., 2014; Mellouki et al., 2015; Schlundt et al., 2017). Photolysis of OVOCs is a primary source of the HO_X ($OH+HO_2$) and organic peroxyl (RO_2) radicals, promoting the production of ozone and peroxyl acetyl nitrate (PAN, $CH_3C(O)OONO_2$) (Singh et al., 1995; Liu Z et al., 2010, 2012). Ozone has adverse effects on human and vegetation health and is a greenhouse gas (Brunekreef & Holgate, 2002; Reich & Amundson, 1985); PAN formation and transport significantly enhance the impact of anthropogenic emissions in remote regions (Fischer et al., 2014; Singh et al., 1981). OVOCs also contribute to the formation of secondary organic aerosols (SOA), which affect human health and regional climate (Kokkola et al., 2014; Hazra et al., 2014; Li J et al., 2016).

Secondary production from the oxidation of nonmethane hydrocarbons (NMHCs) is a major source of OVOCs (Read et al., 2012). However, significant discrepancies were found between surface measurements and model-derived OVOC concentrations from the NMHCs, which are often explained by unknown chemical sources or sinks (Singh et al.,

2000, 2004). Here we show that this degree of discrepancy is strongly affected by the model chemical mechanism and boundary-layer mixing of secondary OVOCs, using the box and 1-D models with explicit and condensed chemistry mechanisms, and observation constraints from the 2014 field campaign at Wangdu in China.

3.2 Data and methods

3.2.1 Wangdu site campaign

The Campaigns of Air Pollution Research in Megacity Beijing and North China Plain (CAREBEIJING-NCP) are made near a small town Wangdu (38.665°N, 115.204°E) in Hebei Province from June 7 to July 8, 2014 (Figure 3.1). Wangdu is not well industrialized. However, major cities including Beijing, Tianjin, and Shijiazhuang locate in a 200km range of the measurement site, as well as multiple coal-fired power plants. The site is expected to be affected by local emissions including uncontrolled coal combustion and biomass burning, as well as regional transport plume in the North China Plain.

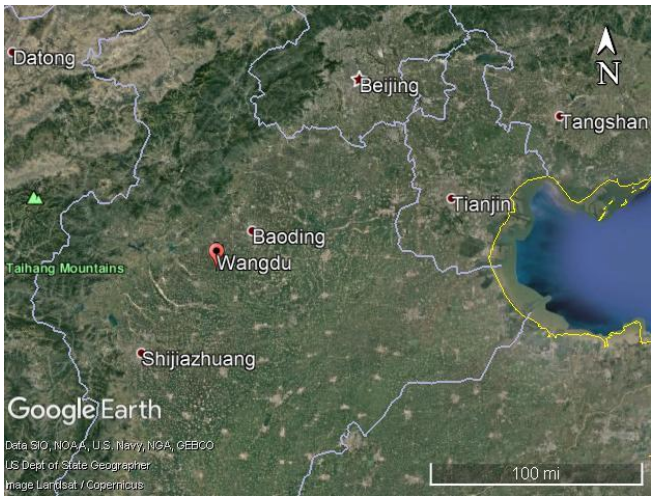

Figure 3.1 Map of Wangdu site and surrounding cities.

Multiple instruments have been adopted in the campaign, and for the same species measured by multiple instruments, we select the data based on accuracy and temporal coverage. O_3 was measured by ultraviolet (UV) absorption (Thermo Electron 49i). CO, CH_4, and H_2O were measured by a cavity ring-down (CRDS) instrument (Picarro G2401). NO and NO_2 were measured by the chemiluminescence method (Thermo Electron 42i). HONO was measured by long-path absorption photometry (LOPAP) using a home-built instrument from Peking University (PKU) (Liu, Y. et al., 2016). 59 VOCs were measured by a gas spectrometer (GC) attached with a flame ionization detector (FID) and a mass spectrometer (MS) from PKU (Wang, M. et al., 2014). Formaldehyde (HCHO) was measured by the Hantzsch fluorescence method (Aerolaser GmbH AL4021). PAN, Cl_2, and $ClNO_2$ were measured by a chemical ionization mass spectrometry (CIMS) instrument from the Georgia Institute of Technology (Liu, X. et al., 2017). OH, HO_2 and RO_2 were measured by laser-induced fluorescence (LIF) technique from PKU (Tan, Z. et al., 2017). The photolysis frequencies were calculated by measured spectral actinic photon flux density using a spectroradiometer (Bohn et al., 2008). The aerosol surface area was calculated by the size distribution of the aerosols measured by a twin differential mobility particle sizer (TDMPS) and an aerodynamic particle sizer (APS) (Wang, Y. et al., 2016). The time resolution and the uncertainties of the measurements used for this study are summarized in Table 3.1.

Table 3.1 Observation methods, time resolution, and uncertainties

	Methods	**Time resolution**	**Uncertainties**	**Reference/Model**
O_3	UV absorption	1 min	5%	Thermo Electron 49i
CO, CH_4, H_2O	CRDS	1 min	5-20%	Picarro G2401

NO, NO_2	chemiluminescence	1 min	20%	Thermo Electron 42i
HONO	LOPAP	0.5 min	20%	Liu, Y. et al., 2016
VOCs	GC-FID/MS	60 min	15-20%	Wang, M. et al., 2014
HCHO	Hantzsch fluorescence	1 min	5%	Aerolaser GmbH AL4021
PAN, Cl_2, $ClNO_2$	CIMS	0.1 min	30-36%	Liu, X. et al., 2017
OH, HO_2, RO_2	LIF	0.5 min	5-12%	Tan, Z. et al., 2017
Photolysis frequency	spectroradiometer	0.33 min	10%	Bohn, B. et al., 2008
Aerosol surface area	TDMPS/APS	10 min	20%	Wang, Y. et al., 2016

3.2.2 Model

As described in CHAPTER 1, the condensed chemical mechanism is taken from the GEOS-Chem mechanism (GCM) with an extension of reactions involving aromatics, ethylene, acetylene, and chlorine with 120 active species and >400 reactions. The explicit chemical mechanism is the Master Chemical Mechanism (MCM 3.3.1) with 3500 species and >10000 reactions. Observed photolysis rates of O_3, NO_2, NO_3, Cl_2, $ClNO_2$, H_2O_2, and HCHO are used in the models. For the other photolysis rates, they are computed using FAST-J module (Wild et al., 2000) and are then linearly scaled using observed O_3 and NO_2 photolysis rates depending on their wavelength dependence. The observations of O_3, CO, CH_4, H_2O, NO, NO_2, HONO, VOCs, HCHO, Cl_2, $ClNO_2$, temperature, pressure, and aerosol surface area are prescribed in the box model and the first layer of the 1-D model. Missing observation data are replaced by the average value at the same time of the day to allow for continuous simulation. The chemistry timestep of the model is 1 minute, and the observations with frequencies lower than once per minute are interpolated linearly.

The 1-D model extends the box model into 30 vertical layers from the surface to the top of the troposphere. The meteorology data including pressure, temperature, water

vapor concentration, and vertical eddy coefficient are obtained from the Weather Research and Forecasting model (WRF) assimilations constrained by the National Centers for Environmental Prediction Climate Forecast System Version 2 (NCEP CFSv2) products (Saha et al., 2013). The additional process in the 1-D model includes vertical mixing and dry deposition (Zhang, Y. et al., 2016; Liu, Z. et al., 2012) based on WRF simulation results. The simulated vertical diffusion coefficient on the surface agrees well with the derivation from the observed surface flux (Figure 3.2). The timestep for vertical mixing is 1 minute, the same as the chemistry timestep.

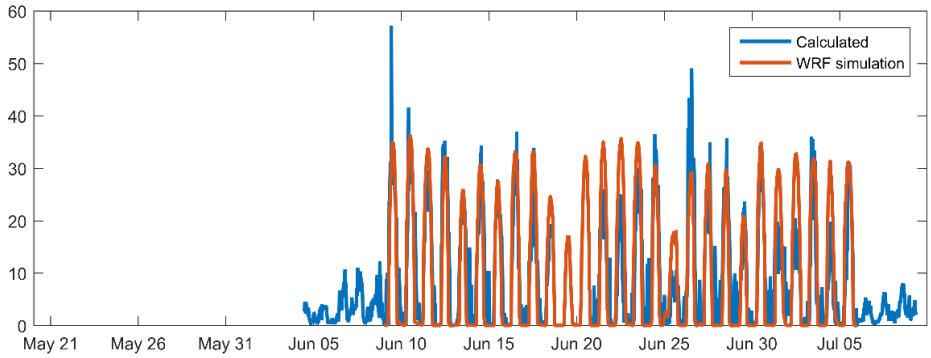

Figure 3.2 The time series of the simulated vertical diffusion coefficient (Kzz) from WRF simulation and the Kzz derived from the observed surface flux.

The dry deposition velocity and the top chemical boundary conditions in the 1-D simulations are obtained from the 3-D REAM model results with the boundary layer height from the WRF simulations. The 3-D REAM model has a horizontal resolution of 36 km, and the vertical resolution of the 3-D REAM is the same as the 1-D model. The chemistry mechanism of the 3-D REAM is the same as the condensed mechanism used in this research. The 2012 Multi-resolution Emission Inventory for China (MEIC) emissions are adopted in the 3-D REAM for anthropogenic emissions of NO_X, VOCs, and CO (Zhang,

Q. et al., 2009). We run the 3-D REAM model for the same period in this study. All models including the box models, 1-D models, and 3-D REAM model are spun up for 10 days for initialization.

3.3 Results and Discussion

3.3.1 Formaldehyde (HCHO), peroxyacetyl nitrate (PAN), and free radicals

Wangdu is a rural site (Figure 3.1), 170 km, 180 km, and 90 km from Beijing, Tianjin, and Shijiazhuang, respectively. However, the in-situ observations during the CAREBEIJING-2014 campaign showed the site was fairly polluted (Wang, Y. et al., 2016; Tan, Z. et al., 2017; Fuchs, H. et al., 2017). We apply box and 1-D model to simulate short-lived daytime HCHO, PAN, and free radical concentrations in light of the observations to understand the effects of boundary layer mixing.

To evaluate model simulated photochemistry, short-lived chemical species are most useful, such as free radicals (Fuchs, H. et al., 2017). HCHO and PAN also have short lifetimes in summer near the surface due to intense sunlight and high temperature, and their observations provide useful constraints on VOC chemistry (Liu, Z. et al., 2012). The daytime (6 AM to 6 PM) variations of OH, HO_2, RO_2, and HCHO are similar in the box and 1-D model but different for PAN due to longer lifetimes of PAN in the upper boundary layer and free troposphere, where temperature lower than the surface. The observed PAN daytime variation reflects the mixing of surface and boundary-layer PAN.

The differences between the box and 1-D models and between MCM and GCM can be more clearly examined by comparing average daytime HCHO, PAN, OH, HO_2, and RO_2

concentrations among the models with the observations (Figure 3.3). The largest difference is found for PAN because of its longer lifetime than HO_X and RO_2 radicals. In general, the MCM mechanism predicted higher concentrations of PAN than GCM. The effect is largest in the box model simulations in which the MCM model overestimates the observations by 161% whereas the GCM results are 14% lower within the uncertainty bound of the observations. The much larger PAN concentrations simulated in the box MCM model than GCM is due largely to higher OVOC production in the former, particularly methylglyoxal, the photolysis of which is a major precursor of PAN (Liu, Z. et al., 2010, 2012). When vertical mixing and deposition processes are included, the 1-D MCM model simulation of PAN is much improved than box model with a 10% overprediction than the observations due mostly to mixing loss of PAN and OVOCs from the surface to the boundary layer.

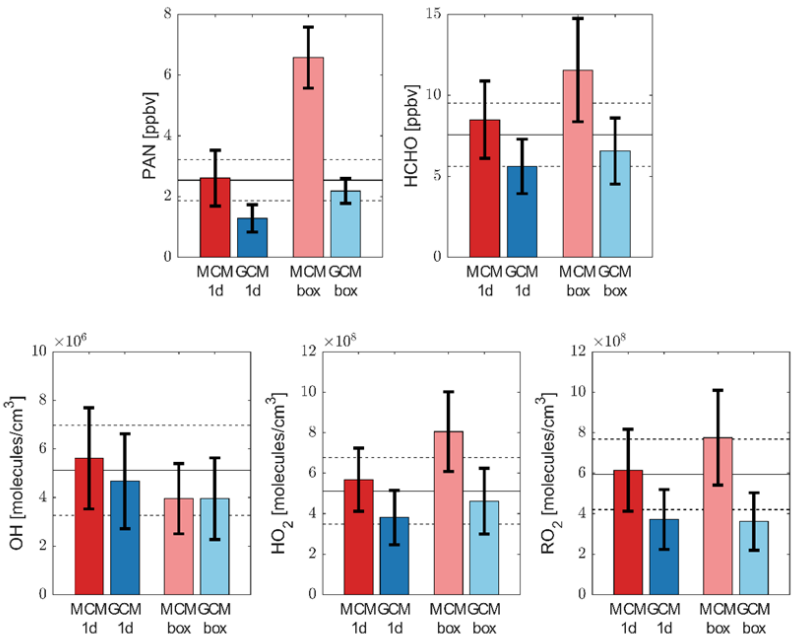

Figure 3.3 Observed and simulated daytime (8 am to 8 pm) average concentrations of (a) PAN; (b) HCHO; (c) OH; (d) HO_2; and (e) RO_2. The solid and dashed black

horizontal lines show the observed mean and standard deviation, respectively. The color bars show the corresponding simulated averages of 1-D MCM, 1-D GCM, box MCM, and box GCM models, respectively, with their standard deviations shown in vertical black lines.

Figure 3.3 shows the daytime mean concentrations of peroxyacetyl nitrate (PAN), formaldehyde (HCHO), OH, HO_2, and RO_2 from the measurements and the surface layer of the models, and the four models show various ability to reproduce the observed values. The observed PAN level is 2.5 ppbv, lower than the summertime observation in other polluted urban regions in China, while much higher than the measurements in background sites (Phillips et al., 2013; Lee et al., 2012; Zhang, G. et al., 2015). The 1-D MCM model has the best performance with the mean concentration 3% higher than the measurement. The 1-D GCM model underestimates 50% of the mean concentration. The box models predicted higher concentrations than the corresponding 1-D models. The box MCM model predicts the highest PAN concentration with the daytime mean value 159% higher than the observation. The box GCM model predicts a 14% lower mean concentration than the observation with the uncertainty covering the observed mean. Besides PAN, OVOCs including HCHO are also critical HO_2 and RO_2 source (Xue et al., 2016; Griffith et al., 2016). The observed level of HCHO is 7.6 ppbv, comparable to the summertime observation in Beijing (Qian et al., 2019), indicating strong local chemical reactivity due to the short lifetime of the HCHO. The 1-D MCM slightly overestimates the HCHO by 12% with the best performance. The 1-D GCM model underestimates HCHO for 26%. The box MCM model again overpredicts the HCHO for 53%, while the box GCM model has a fair result by underestimating 13%. The results show that the chemical process in the box MCM model tends to be too strong while in the 1-D GCM model, the chemical activities are too weak.

3.3.2 The photoreactivity of the OVOCs and the radicals

While the MCM mechanism contains ~900 more kinds of OVOC species than the GCM mechanism, most of the unique species in the MCM mechanism are alcohols and carbonyls with 4 or more carbon atoms, which are less active than the common species in both mechanisms, making the comparison of the total OVOC concentration less convincing. To examine the contribution of the OVOCs to the chemical process, we separate the OVOCs by common species in both mechanisms and unique species in each mechanism, and we calculate their the mean daytime OVOCs photolysis rate (Figure 3.4a) and OVOCs photolytic production of HO_2 (Figure 3.4b) and RO_2 (Figure 3.4c) radicals in the surface layer of the four models. The total photolysis rate on the surface in the 1-D MCM model is 1.6 ppbv h^{-1}, higher than the 1.0 ppbv h^{-1} in the 1-D GCM model. The common species provide 1.4 ppbv h^{-1} (89%) in the 1-D MCM mechanism, 39% higher than the GCM mechanism, mostly due to formaldehyde (HCHO) and methylglyoxal (MGLY). The total photolysis rate of OVOC is much higher in the box models than the surface in 1-D models, despite the constrained photolysis rate used in all models, implying a higher concentration of the OVOCs in the box models than the corresponding 1-D models. The total photolysis rates of OVOCs in the box models are 3.0 ppbv h^{-1} and 1.4 ppbv h^{-1} for box MCM and GCM mechanisms respectively. The common species contribute 2.6 ppbv h^{-1} (89%) in the box MCM model, 86% higher than the box GCM model. HCHO and MGLY remain the most significant contributor to the total photolysis rate.

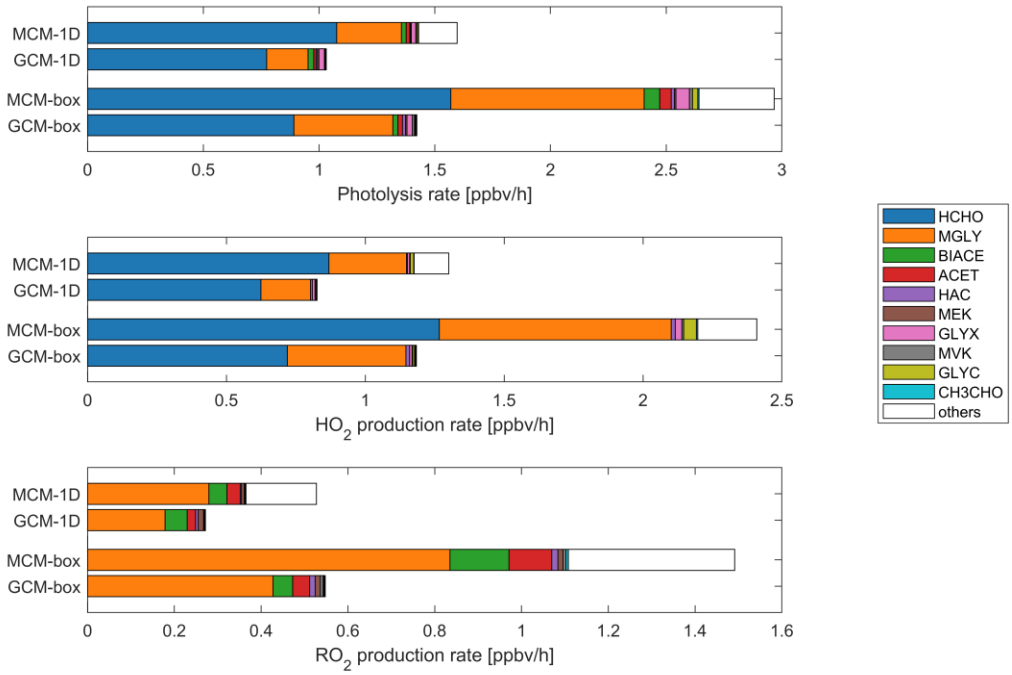

Figure 3.4 daytime means results from the surface layer of the 1-D models and the box models for (a) total OVOC photolysis rate; (b) HO_2 production rate from photolysis of OVOCs; and (c) RO_2 production rate from photolysis of OVOCs. Common species in the two mechanisms are colored, and unique species are left white. The common species are formaldehyde (HCHO), methylglyoxal (MGLY), biacetyl (BIACE), acetone (ACET), hydroxyacetone (HAC), methyl ethyl ketone (MEK), glyoxal (GLYX), methyl vinyl ketone (MVK), glycolaldehyde (GLYC), and acetaldehyde (CH3CHO).

The HO_2 productions from the photolysis of OVOCs in the four models have a similar composition to the photolysis rate. The total photolytic HO_2 production rate is 1.3 ppbv h^{-1} in the 1-D MCM model, and 0.8 ppbv h^{-1} in the 1-D GCM model, while we see high values of 2.4 ppbv h^{-1} in the box MCM model, and 1.2 ppbv h^{-1} in the box GCM model. The common species contribute 1.2 ppbv h^{-1} (91%) in the 1-D MCM model and 2.2 ppbv h^{-1} (91%) in the box MCM model, while in the GCM models, the common species contribute all the HO_2 production. The most notable species is still HCHO and MGLY, and

both their HO_2 photolysis yields are ~1. However, the RO_2 photolytic productions are quite different from the photolysis rate or the HO_2 photolytic production. The RO_2 production rates in the models are 0.5 ppbv h^{-1} for the 1-D MCM model, 0.3 ppbv h^{-1} for the 1-D GCM model, 1.5 ppbv h^{-1} for the box MCM model, and 0.6 ppbv h^{-1} for the box GCM model. The HCHO provides no RO_2, and the most important RO_2 producing OVOC is the MGLY. The contribution of biacetyl (BIACE) and acetone (ACET) rises dramatically due to their higher yield of RO_2. The contribution of the common species is 0.4 ppbv h^{-1} (70%) for the 1-D MCM model and 1.1 ppbv h^{-1} (74%) for the box MCM model. The lower contribution of the common species in the RO_2 production rate than the HO_2 production rate in the MCM models implies that the unique species in the MCM mechanism mainly impact the chemical activity through RO_2 radicals.

While we have observed lower RO_2 concentrations in the GCM models than the MCM models (Figure 3.4), due to the complexity of the RO_2, the reactivity varies. To assess the contribution of the RO_2 to the photochemistry activity, we examine the ozone production rate in the models, i.e., the oxidation speed of NO by HO_2 and RO_2 radicals (Kleinman et al., 2002). Figure 3.5 shows the mean daytime ozone production rate in the ground layer of the 1-D models as well as in the box models. The total ozone production rate in the 1-D MCM model is 14.9 ppbv h^{-1}, 91% higher than the 7.8 ppbv h^{-1} in the 1-D GCM model. The RO_2 contributes 7.2 ppbv h^{-1} (49%) and 3.4 ppbv h^{-1} (44%) in the 1-D MCM model and 1-D GCM model separately, showing that the RO_2 radical is much more active in the MCM mechanism. A similar ratio can be found in the box models. In the box MCM model, the RO_2 radical contribute 9.5 ppbv h^{-1} (47%) of the total ozone production rate of 20.4 ppbv h^{-1}. In the box GCM model, the RO_2 radical contribute 4.1 ppbv h^{-1} (41%)

of the overall ozone production rate of 10.1 ppbv h^{-1}. The GCM mechanism not only underestimates the total ozone production rate but also underestimate the relative contribution of the RO_2 radicals.

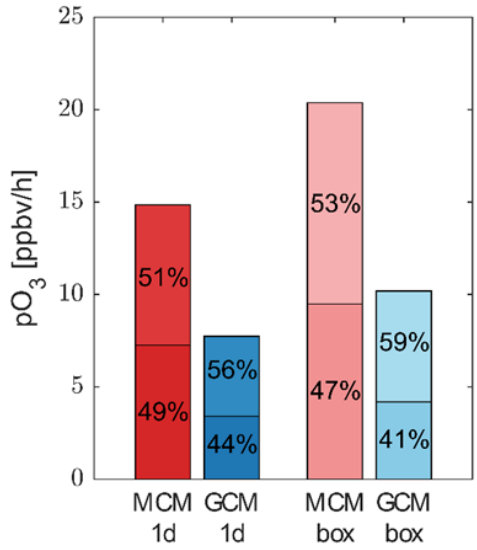

Figure 3.5 Simulated daytime means of the ozone production rate of the ground layer in the 1-D MCM model, the ground layer in the 1-D GCM model, the box MCM model, and the box GCM model from left to right.

3.4 Implications

The box model is often used for case studies based on measurements (Karl et al., 2018; Lu et al., 2013; Liu, X. et al., 2017), and both the condensed mechanism and the explicit mechanism can be assembled into the model. Although the condensed mechanism is more comprehensive, without proper vertical structure, the model would predict massive OVOCs and radicals. The vertical transport is a substantial loss process for species produced on the ground level and decaying over altitude, especially in the daytime where the vertical mixing is strong (Lin et al., 2010). The absence of such a process would result in an accumulation of the species while the effect depends on their chemical lifetime. Short

lifetime species such as the radicals are barely affected by the transport process, as the radicals are very chemical active with fast formation and loss rate. However, their precursors – the OVOCs – usually have lifetimes of several hours (Fu et al., 2008; Lee et al., 1995), which allows them to be strongly affected by vertical transport. In the box model where there is no vertical transport, the OVOCs concentrations are largely overestimated and consequently giving an overestimated total OVOC reactivity and overestimate PAN, HO_2, and RO_2 levels. To correctly evaluate the chemical reactivity in the circumstance, we need to use the explicit mechanism with a proper vertical structure.

The condensed chemical mechanism has been widely adopted in 3-D models that are used for evaluating the pollutant control measurements, for studying regional and global atmospheric chemical activities, and for estimating the budget (Zhang, R. et al., 2017; Yang et al., 2011). With the evidence of underestimated OVOCs in the condensed mechanism, we can expect that the ozone production rate is also less sensitive to NO_X emission due to the lower VOC/NO_X ratio than the explicit model (Seinfeld & Pandis, 2006). Figure 3.6 illustrated the change of ozone production rate to the change of NO_X emission over the boundary layer in the 1-D models with the two mechanisms. The ozone production is less and less sensitive to the NO_X emission as the NO_X emission increases in both models. However, the sensitivity is 50% to 120% higher in the MCM mechanism than in the GCM mechanism, indicating an underestimated sensitivity of ozone production to the NO_X emission in the condensed mechanism. With models using the condensed mechanism, the NO_X control measurements are less favored, and the enhancement of ozone formation by new NO_X emission is underrated, which would result in biased control measures and solutions. The concentration and the chemical reactivity of the OVOCs in

the condensed mechanism are also underestimated, which can cause an underestimated surface OVOCs flux and OA yield from existing NMHCs in the model, leading to significant error in budget estimation.

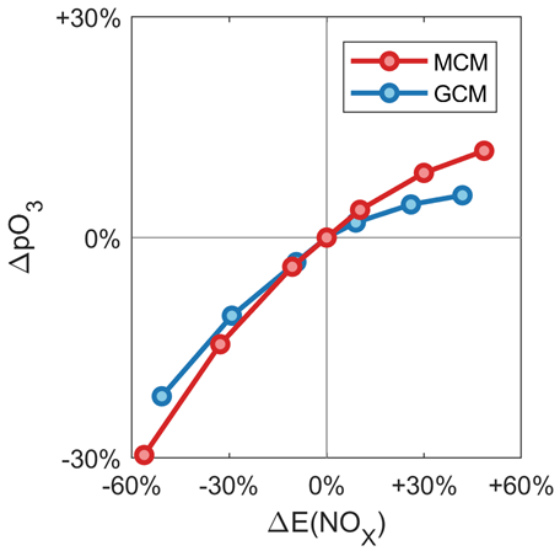

Figure 3.6 The sensitivity of boundary layer daytime mean ozone production rate to the NO_X emission in two 1-D models. The red line shows the results from the 1-D MCM model, and the blue line shows the results from the 1-D GCM model.

CHAPTER 4. CITY-SCALE NO_X EMISSION ESTIMATION FROM FITTING HIGH-RESOLUTION SATELLITE COMPOSITE DATA: UNCERTAINTY FACTORS

4.1 Introduction

Nitrogen oxides (NO_X) are toxic pollutants in the atmosphere and act as precursors for tropospheric ozone and secondary aerosols (Gu et al., 2016; Zhang, R. et al., 2018). The combustion processes in power plants, vehicles, and factories are dominating anthropogenic sources of the NO_X (Li et al., 2019). An accurate inventory for the NO_X emission is critical for predicting the tropospheric ozone level as well as evaluating the pollution control measurements. The bottom-up emission inventories of NO_X usually have significant uncertainties due to changing emission factors and the limited information and resolution of the source data (Zhao et al., 2011). Satellite observation, on the contrary, provides a global view of the NO_2 column concentration with minor uncertainty and can be used for trend analysis or derivation of accurate top-down NO_X emissions through inverse modeling or direct methods (Gu et al., 2013; Lamsal et al., 2008; Qu et al., 2019; Wang et al., 2010).

The exponentially modified Gaussian (EMG) fitting is one of the most commonly used methods deriving lifetimes and emissions directly from the satellite observation. This method combines the Gaussian distribution from the diffusion process and the exponential decay from first-order chemical loss. Beirle et al. (2004) first adopted the EMG for estimating the ship NOx emission from the Global Ozone Monitoring Experiment (GOME)

observed the NO_2 column on the Indian ocean. Beirle et al. (2011) revise the method by separating the observation by wind direction on estimating the total NOx emission from Riyadh, Saudi Arabia from the Ozone Monitoring Instrument (OMI) observed NO_2. Valin et al. (2013) further improve the method by rotating the satellite observation by the wind direction and analyses the impact of wind speed on estimated NOx lifetime and emission, suggesting that under high wind speed conditions, the estimation is less affected by the wind variability and more convincing. The EMG method with rotation has been applied to analyze emissions from satellite observation of various species (Fioletov et al., 2015; Goldberg et al., 2019; Laughner et al., 2015; Lu et al., 2015). The performance of the EMG fitting method has been evaluated by de Foy et al. (2014, 2015), applying on the simulated column with known lifetime and emissions from a point source. The emission estimation is found most accurate at high wind speed, and the results are quite stable. Liu, F. et al. (2016) further modify the method by substitute the Gaussian function by the distribution of NO_2 line density under the calm wind condition to estimate the lifetime, and Liu, F. et al. (2017) use the new method to derive the emissions from 48 China cities.

Although the uncertainty of the EMG fitting process has been characterized, the impact of the satellite sampling process on the accuracy of the EMG method remains unknown. In this study, we evaluate this impact by comparing the fitted emission before and after the satellite resampling with the pixels from the OMI satellite as well as the newly launched TROPOspheric Monitoring Instrument (TROPOMI) satellite. We apply the method on both an ideal EMG shaped NO_2 plume from a point source and a simulated NO_2 plume modeled by the Community Multi-scale Air Quality (CMAQ) model over the Yangtze River Delta region.

4.2 Data and Methods

4.2.1 OMI/TROPOMI satellite and the resampling process

The OMI satellite was launched in July 2004, observing trace gases and aerosols with a resolution of 13 × 24 km^2 at nadir. In this work, we used the level 2 data from the Dutch OMI NO_2 (DOMINO) v2.0 product (Boersma et al., 2011). This product has been widely adopted for the EMG fitting as well as for NO_X emission inversion (Vinken et al., 2014; Lamsal et al., 2015). In this research, we used the location data (corner longitude and latitude) of the satellite pixels rather than the NO_2 total column observed by the satellite. We obtain a total of more than 94,200 pixels of OMI observation over the Yangtze River Delta region in June, July, and August in 2014. We applied no filter on the pixels.

The TROPOMI satellite was launched in October 2017, focusing on similar species as the OMI satellite with a higher resolution of 7 × 3.5 km^2 at nadir. The TROPOMI NO_2 processing system has the same algorithm as the DOMINO v2.0 product, except that it has been adapted for TROPOMI (http://www.tropomi.eu/data-products/nitrogen-dioxide). We applied the same process on the TROPOMI pixels in June, July, and August in 2018. The total number of TROPOMI pixels exceeds 1,200,000 over the same region.

For each satellite pixel, we calculated the resampled NO_2 column for the pixel by averaging the NO_2 column in the grids it fully or partly covers weighted by the common area of the two, in Eq 3.1:

$$R = \frac{\sum(VCD_i \times A_i)}{\sum A_i} \quad \text{(Eq 3.1)}$$

where R is the resampled NO_2 column value for the satellite pixel, VCD_i are the NO_2 vertical column density in grid i, and A_i is the common area between grid i and the satellite pixel. In this way, the total NO_2 amount is preserved inside the satellite pixel.

4.2.2 EMG fitting of a city-scale plume

In Beirle et al. (2011), the Exponential Modified Gaussian function that characterizes the distribution of the line density over the wind direction comes from the combination of the Gaussian distribution $G(x)$ that describes the diffusion process in Eq 3.2 and the exponential decay function $e(x)$ that represents the first-order chemical loss in Eq 3.3:

$$G(x) = \frac{1}{\sqrt{2\pi}\sigma_x} \exp\left(-\frac{x^2}{2\sigma_x^2}\right) \quad \text{(Eq 3.2)}$$

$$e(x) = \exp\left(-\frac{x-P}{x_0}\right) I_{(x>P)} \quad \text{(Eq 3.3)}$$

where σ_x is the standard deviation in the x-direction (wind direction), P is the location of the emission source, x_0 is the e-folding distance of the chemical decay, and I is the indicator function. The EMG function is then interpreted as Eq 3.4:

$$M(x) = E \exp\left(-\frac{x-P}{x_0} + \frac{\sigma_x^2}{2x_0^2}\right) \Phi\left(\frac{x-P}{\sigma_x} - \frac{\sigma_x}{x_0}\right) + B \quad \text{(Eq 3.4)}$$

E is the total emission of NO_2 in this region, Φ is the cumulative distribution function of the standard normal distribution, and B is a constant background. In this study, we substitute the parameter E with L/x_0, so the EMG equation becomes Eq 3.5:

$$M(x) = \frac{L}{x_0}\exp\left(-\frac{x-P}{x_0}+\frac{\sigma_x^2}{2x_0^2}\right)\Phi\left(\frac{x-P}{\sigma_x}-\frac{\sigma_x}{x_0}\right)+B \quad \text{(Eq 3.5)}$$

It is easy to see that L is the total amount of NO_2 above the background as we can integrate both sides on Eq 3.5, we get Eq 3.6:

$$\int_{-\frac{d}{2}}^{\frac{d}{2}}[M(x)-B]dx = L \quad \text{(Eq 3.6)}$$

In the fitting, we rotate the data to align the wind direction into the x-direction and calculated the line density by integral the NO_2 column in the y-direction from -d/2 to d/2 (d is the cross-section integral distance). The center grid of the rotation for the CMAQ simulation and its resampling results are chosen according to the emission inventory. Then we perform a least-square curve fitting of the line density to fit the parameters σ_x, P, x_0, L, and B, and further derive NOx lifetime ($\tau=x_0/w$) and NOx emission ($E=(1.32\times L)/\tau$), where w is the mean wind speed.

4.2.3 CMAQ model and ideal plume

Simulations are conducted for three nested grids with a horizontal resolution of 36 km (D1), 12km (D2), and 4km (D3), respectively (Figure 4.1). D1 covers most of China and the surrounding countries including Japan and South Korea; D2 covers eastern China and D3 covers the entire YRD region and its surrounding land and waters. Meteorological fields are provided by the Weather Research and Forecasting (WRF version 3.7, Skamarock et al., 2008) model with 27 vertical layers extending to the tropopause (100hpa). WRF initial and boundary conditions (ICs, BCs) are based on the 1° x 1°

reanalysis data from the National Centers for Environmental Prediction Final Analysis (NCEP-FNL).

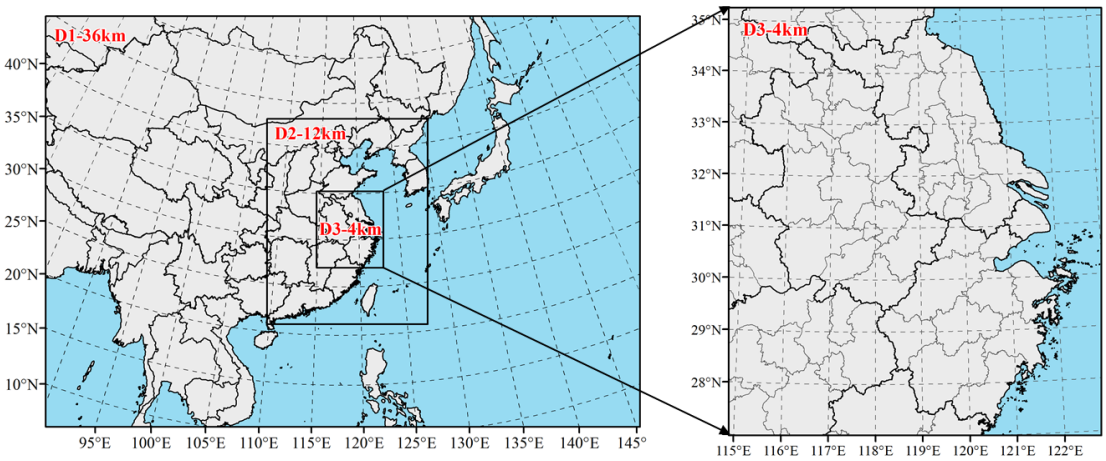

Figure 4.1 Three nested model domains. The resolutions of the three domains are 36 km, 12 km, and 4 km for D1, D2, and D3 separately.

Anthropogenic emissions in YRD are updated based on a most recent inventory (Huang et al., 2011; Li et al., 2011; Liu, Y. et al., 2018). Emissions for areas outside YRD in China are derived from the Multi-resolution Emission Inventory for China (MEIC) emissions model for 2012 (Zhang et al., 2009) and anthropogenic emissions of other regions are from the Model Inter-Comparison Study (MIX) emission inventory for 2010 (Li et al., 2017). Biogenic emissions are estimated by Model of Emissions of Gases and Aerosols from Nature (MEGAN) v2.1 (Guenther et al., 2012) using WRF meteorology predictions. The Sparse Matrix Operator Kernel Emissions (SMOKE, https://www.cmascenter.org/smoke) model is applied to process emissions for input to CMAQ.

CMAQ version 5.0.2 (https://www.cmascenter.org/cmaq/) is used to simulate atmospheric pollutants concentrations. ICs and BCs of D1 domain are based on a Model

for Ozone and Related Chemical Tracers (MOZART) global simulation (https://www.acom.ucar.edu/wrf-chem/mozart.shtml). For the inner D2 and D3 domain, ICs and BCs are extracted from the simulation results of the outer domains.

In addition to the CMAQ simulation, we generated two ideal plumes under west wind and south wind conditions separately, as southwest is the dominant wind direction in the research period. The emission center of the plume is Shanghai, the largest city in the YRD region. The line density along the wind direction of the plumes follow EMG function with no background concentration, and the across the wind direction, the plumes follow a Gaussian distribution, as in Eq 3.7:

$$IP(x,y) = M(x) \times \frac{1}{\sqrt{2\pi}\sigma_y} \exp\left(-\frac{\left(y - P_y\right)^2}{2\sigma_y^2}\right) \quad \text{(Eq 3.7)}$$

where σ_y and P_y are the standard deviation and source position in the y-direction. The parameters we use for generating the plumes are in Table 4.1.

Table 4.1 Parameters used in the generation of the idealized plume

Parameter	L	x_0	σ_x	σ_y	P_x	P_y	w	τ	E
Value	1×10^{27} molecules	40 km	10 km	10 km	0 km	0 km	10 km h^{-1}	4 h	3.3×10^{26} molecules h^{-1}

4.3 Results

4.3.1 Idealized city plume

Figure 4.2 shows the distribution of the ideal plume and the resampled plume under the west wind and the south wind. The OMI satellite resampling process significantly

shifted the shape of the plume. Comparing to the original plume, the OMI resampled plume stretches in the east-west direction, causing a longer tail in the west wind case and a wider distributing range in the south wind case. Also, in the resample plume, the NO_2 density at the center of the emission is 45% and 58% lower than the ideal plume for the west wind case and the south wind case separately, indicating that the OMI satellite results massively underestimate NO_2 column in the emission center. Both the effects are due to the rough resolution of the OMI satellite, which averages the NO_2 column over a broad range and reduces its gradient, especially in the east-west direction where the rectangular-shaped OMI pixel is longer (refer to Figure 4.3 for example). The TROPOMI satellite resampling process, on the contrary, maintains the original distribution with only 7% decay of the NO_2 density in the emission center.

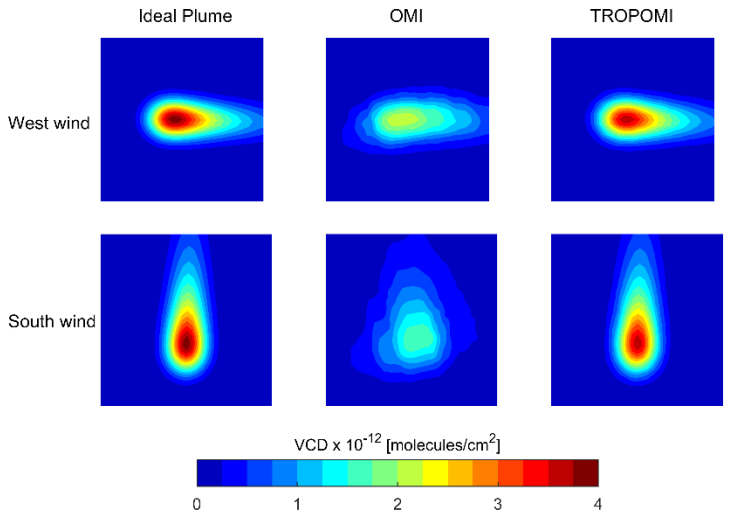

Figure 4.2 The generated ideal plume and the resampled ideal plume by OMI satellite pixels and TROPOMI satellite pixels

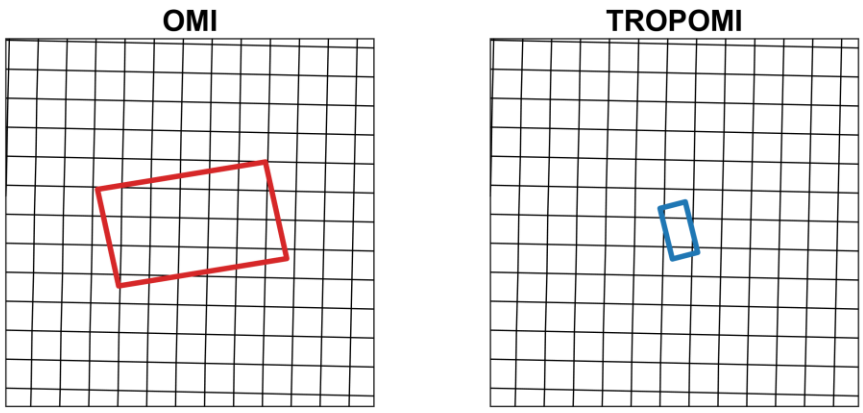

Figure 4.3 Illustration of one nadir OMI (left in red) pixel and one nadir TROPOMI (right in blue) pixel over the 4-km grids (black) in the CMAQ model covering the same location. The topside is north. The OMI pixel covers ~20 grids while the TROPOMI pixel merely covers 2 grids. The OMI pixel is much longer in the east-west direction than the north-south direction

We applied the EMG fitting on all plumes under various integral distances. Figure 4.4 shows the relative error of the estimated parameters. The accuracy of the fitted total NO_2 amount T, and NO_X emission E showed great dependency on the integral distance. The underestimation of the total NO_2 amount T due to the part of NO_2 transport out of the integral range, and as the range increases, the fraction is smaller. The underestimation of total NO_2 drops to 0 at around 60km for the idealized plume and the TROPOMI resampled plume in both wind direction, corresponding to the $3\sigma_y$ on two sides. The OMI resampled plume yields an extra error in the total NO_2 amount estimation, and the extra error depends on both the wind direction and the integral distance. In the results from the OMI resampled plume, the total NO_2 amount is underestimated for an extra 10% in the west wind case and 20% in the south wind case than the idealized plume fitting results under the integral

distance of 10 km. However, as the integral distance increases, the underestimation disappears for the west wind case after 70 km, while in the south wind case, the underestimation drops to 10% at an integral distance of 100 km. The underestimation is related to the rough resolution of the OMI pixel. While the resampling process preserves the total NO_2 amount inside the satellite pixel, it will remove any gradient inside the pixel, which is equivalent to moving NO_2 from high concentration area to low concentration area inside the pixel. In this specific idealized plume case, if a satellite pixel covers the edge of the integral region, the outer part will always have a lower NO_2 concentration than the inner part, and the resampling process will move NO_2 out of the integral range and cause underestimation. The OMI satellite has a much larger pixel size than the TROPOMI, making more OMI pixels covering the edge and leads to higher underestimation. Also, as the OMI satellite pixels are longer in the west-east direction than in the south-north direction, more pixels cover the edge of the integral area in the south wind case than in the west wind case, causing a higher error.

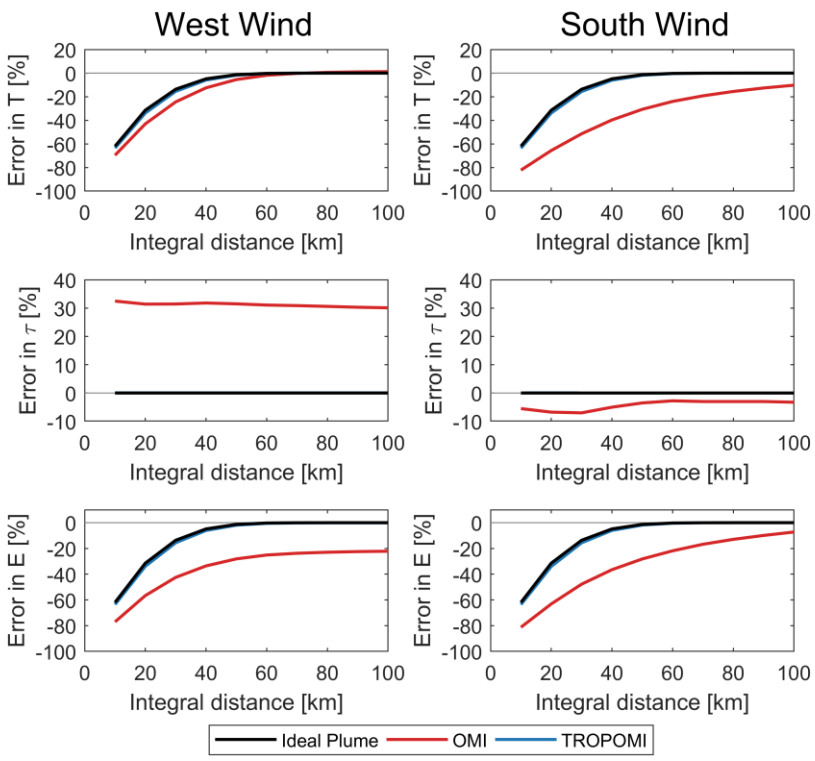

Figure 4.4 The relative error changing with the integral distance in the total amount of NO_X (T), lifetime (τ), and emission (E) in the ideal plume and the OMI and TROPOMI resampled ideal plumes

The lifetime estimation is much more accurate for the idealized plume and the TROPOMI resampled plume, with differences under 1%. The OMI resampled plume also yields a 30% longer lifetime for the west wind case and 3-7% shorter lifetime for the south wind case, and the bias is uncorrelated to the integral distance. The error in NO_2 lifetime estimation is more complicated than the total NO_2 amount as the e-folding distance x_0, which is the traveling distance of air in one lifetime, determines the distribution of the NO_2 column line density together with the diffusion coefficient in x direction. Still, the higher error in the OMI results than the idealized plume or TROPOMI plume indicates that the bias in lifetime depends on pixel size of the satellite.

The estimated emission is then calculated by dividing estimated total NO_2 by lifetime. Both the idealized plume and the TROPOMI resampled plume has accurate lifetime estimation and the bias in the emission follows the bias in the total NO_2 amount, ranging from 60% to 0% with the cross-wind integral distance changing from 10km to 60km, and after 60km the emission estimation is precise. The OMI resampled plume, however, underestimate the emission for 80% to 20% in west wind case and 80% to 10% in south wind case. The bias in the emission estimation is a combination of the errors in the estimations of total NO_2 amount and lifetime. As the error in lifetime is independent of the integral distance, the accuracy of the OMI satellite resampled plume is limited.

The results from the resampled ideal plumes indicate that the cross-section integral distance is an important factor in the EMG method, and the accuracy is approving with longer integral distance. However, the idealized plume only considered a point source without interference from other sources, and we further investigate the effect of the integral distance based on CMAQ simulated NO_2 columns.

4.3.2 CMAQ simulation

Figure 4.5 illustrates the mean NO_2 tropospheric column for July and August in the Yangtze River Delta area from the CMAQ simulation and its resampled results with the pixels of the OMI satellite and the TROPOMI satellite under 4 km resolution. The distribution of the CMAQ simulation clearly shows the point sources and their outflow under the dominating southwest wind. The 95th percentile of the NO_2 column in the CMAQ simulation is 1.29×10^{16} molecules cm^{-2}. The OMI satellite resampled result obscures the distribution of the NO_2 column, significantly lowering the NO_2 column

density in the high concentration areas, making the small point sources indistinguishable from the background. The 95th percentile of the NO_2 column in the OMI resampled results is 8.33×10^{15} molecules cm^{-2}, 36% lower than the original CMAQ result. The TROPOMI resampled result mostly preserves the distribution of the original NO_2 column. However, for areas with a high NO_2 concentration gradient, the smoothing effect is visible, and the 95th percentile of the NO_2 column slightly drops to 1.25×10^{16} molecules cm^{-2}.

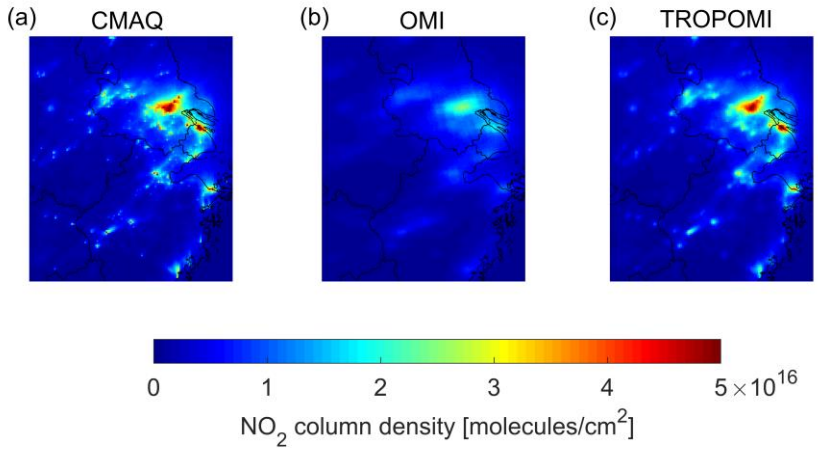

Figure 4.5 (a) Simulated CMAQ NO_2 columns; (b) the resampled NO_2 columns by OMI satellite pixels; (c) the resampled NO_2 columns by TROPOMI satellite pixels.

We choose two areas with the highest NO_2 column density in the CMAQ simulation for the EMG fitting: the Nantong area and the Shanghai area (Figure 4.6). The distance between the center of the two regions is 105km. Although the EMG function only represents the plume from point sources, here we applied the EMG fitting to the two areas to examine the possible bias in the results. As previous researches have also indicated that the wind speed threshold will impact the accuracy of the fitting (Laughner et al., 2016; Lu et al., 2015), we in addition group the data by the wind speed, with calm condition of wind

speed <4 m s^{-1} and windy condition of wind speed $\geqslant$ 4 m s^{-1}, and we apply EMG fitting for each group separately.

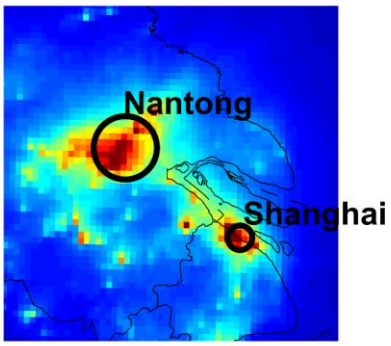

Figure 4.6 Location of Shanghai and Nantong. The Nantong region has a broader distribution range of high NO_2 column pixels than the Shanghai region

Figure 4.7 shows the rotation results under the calm wind condition. The average wind speed in Shanghai is 2.83 m s^{-1}, and the average wind speed in Nantong is 2.82 m s^{-1}. Under calm wind condition, the horizontal transport of NO_2 is limited, and the distribution of the NO_2 column generally follows the distribution of the emission. In Shnaghai, the shape of the plume indicates that the local NO_X emission is concentrated at the center. In Nantong, the band of high concentration plume indicates that the local NO_X emission is spreading over the surrounding region.

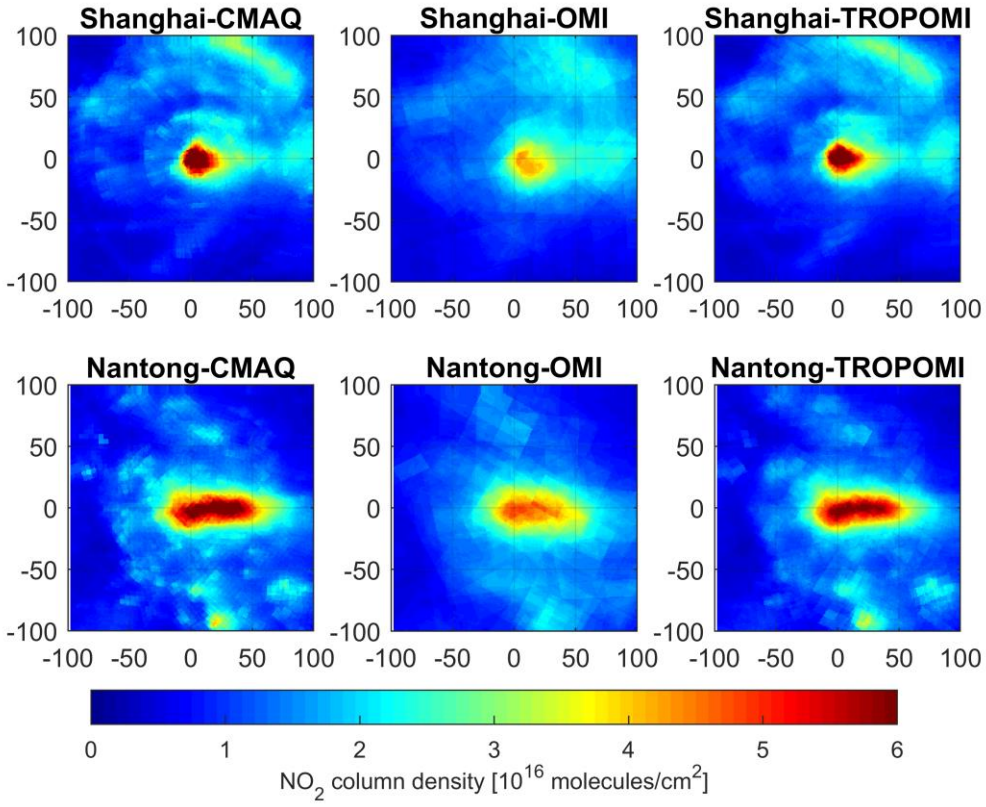

Figure 4.7 Monthly mean of the NO_2 column density after rotation by wind direction, under calm wind condition (<4 m s^{-1})

We applied the EMG fitting on the calm wind plume, and the relationship between the fitted lifetime and emission to integral distance is shown in Figure 4.8. The difference between the fitting results of CMAQ simulation and the TROPOMI resampled plume is small, indicating the consistency of the TROPOMI resampling process under the 4km resolution. The OMI resampled plume generally yields a higher lifetime than the CMAQ plume and the TROPOMI resampled plume, consistent with the ideal plume results under west wind condition. In Shanghai, the estimations of lifetime are stable for CMAQ and TROPOMI, but for OMI the lifetime estimation increases with integral distance. The lifetime estimated from the CMAQ or TROPOMI appears to be too short compared to the

3-4h lifetime in other studies using the same method on OMI observations (Beirle et al., 2004, 2011; Liu, F. et al., 2016, 2017). However, the reason behind the underestimation is the false assumption of the constant lifetime in the EMG function, while the lifetime of NO_2 positively correlates to its concentration if the NO_2 level is high (Zhang, R. et al., 2018; Gu et al., 2014, 2016). Under the calm wind condition, the NO_2 accumulates on where the emissions are, so the lifetime of NO_2 in the center of the emission is very high. In the downwind direction where the NO_2 concentration drops, the lifetime of NO_2 also decreases, creating a much stronger gradient along the wind direction than the constant lifetime would form. When fitting with the EMG function, it explains the strong gradient by a short constant lifetime, causing the underestimation. For the OMI result, as the OMI resampling process smooths the distribution to a wider area, the sharp gradient is lowered such that the estimated lifetime can be longer. However, the smoothing effect also brings in NO_2 from further sources, when the NO_2 from Nantong begins to interfere with the OMI results, the estimated lifetime rises to explain the extra NO_2 in the downwind direction. This phenomenon is missing in Nantong as the Shanghai emission is concentrated in a small region. In Nantong, the estimated lifetime from the plumes are higher than that in Shanghai, and the lifetime estimation has no apparent trends. The consistent lifetime estimation in Nantong is due to the area source like emissions. Under the calm wind condition, the distribution of the area source contributes much more to the shape of the NO_2 line density than the chemical decay and diffusion.

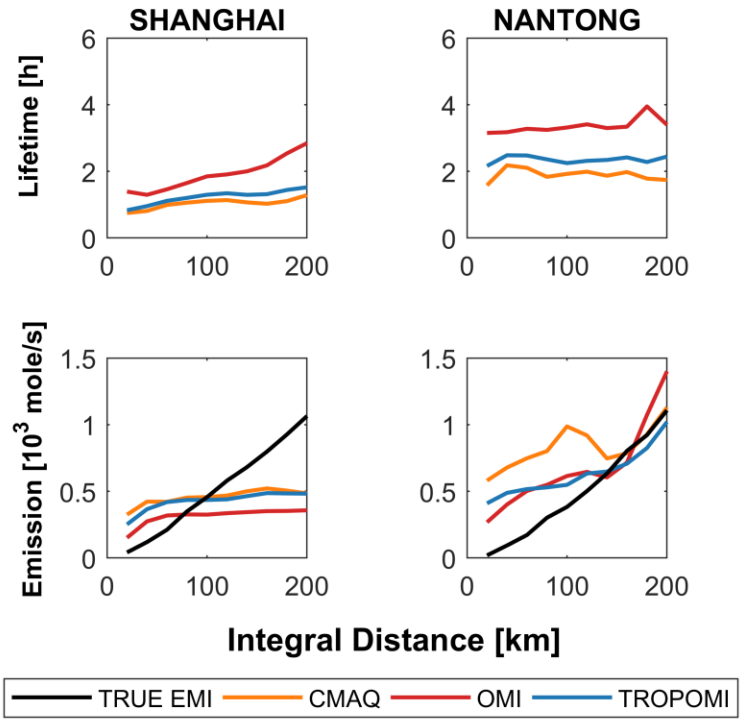

Figure 4.8 The correlation of EMG fitting result of the lifetime and the total emission to integral distance for Shanghai and Nantong under calm wind condition

The NO_2 emission is fitted in the model and compared to the emission inventory we used in the CMAQ simulation. In both Shanghai and Nantong, the accuracy of the fitted emission largely depends on the integral distance. In Shanghai, the emissions are overestimate at a integral distance of 20-60 km for OMI plume, and 20-80 km for CMAQ and TROPOMI plume. After 80km, the fitted emissions almost remain in the same level due to the stable estimation of the lifetime, and the concentrated distribution of the NO_2 column around Shanghai. However, the true emission in the model input keeps on increasing. In Nantong, the accuracy also depends on the integral distance, with the fitted

emission higher than the true emission under 140 km. After 140km, the fitted emission increase with the integral distance with similar rate as the true emission.

Figure 4.9 shows the rotation results under the windy condition. The average wind speed in Shanghai is 6.6 m s^{-1}, and the average wind speed in Nantong is 5.8 m s^{-1}. The horizontal transport due to the wind is clearly visible. In both Shanghai and Nantong, the NO_2 is blown downwind, leaving a long tail extends to more than 100 km. However, the large pixel of the OMI satellite creates blocks of high NO_2 columns on the figure, and the tail of the plume is hard to distinguish from the background.

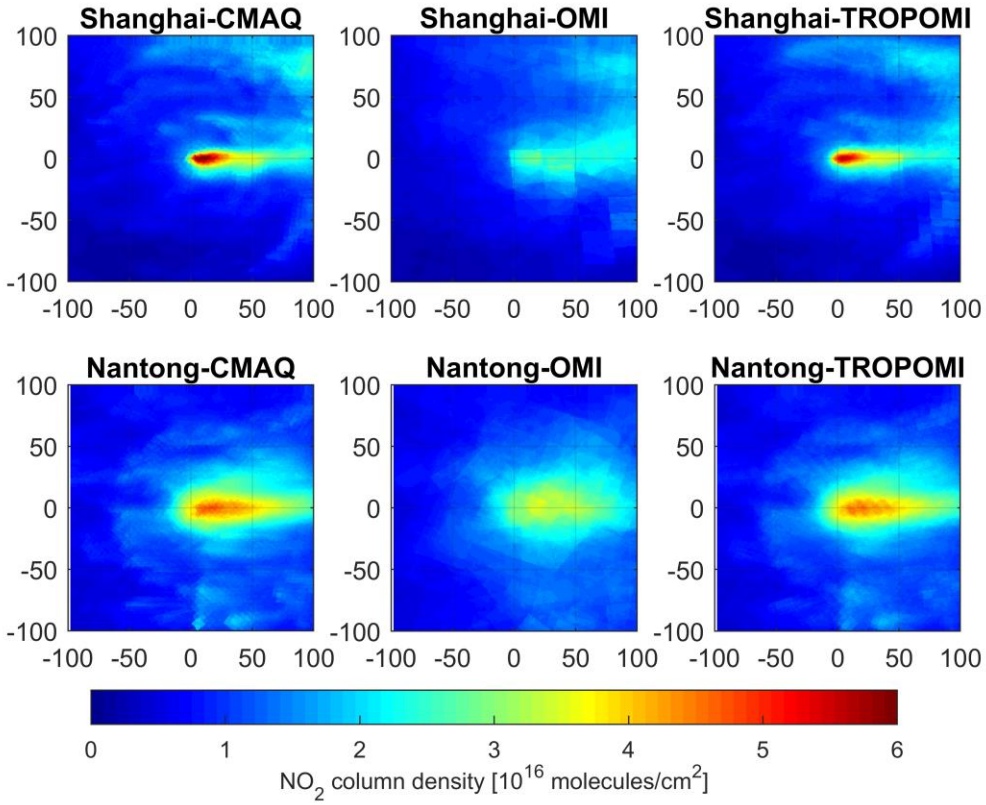

Figure 4.9 Monthly mean of the NO_2 column density after rotation by wind direction, under windy condition (>4 m s^{-1})

Figure 4.10 shows fitting results under the windy condition. In contrast to the dispersed results under the calm condition, the CMAQ model simulation and the TROPOMI resampled plumes yield very similar fitting for both lifetime and emission. In Shanghai, the lifetime estimation for CMAQ and TROPOMI plume is stable at ~ 1.8 hours, while the lifetime estimation for the OMI plume has discontinuous points where the relationship of the lifetime estimation to the integral distance turns over. In Nantong, all three plumes yield a much longer lifetime than Shanghai or Nantong under calm wind condition. The emission estimation for Shanghai is only accurate at an integral distance of 20-40km for OMI, or 40-60km for CMAQ and TROPOMI. After 60km, the estimated emissions remain the same level similar to the calm wind condition, and the method fails. The emission estimation in Nantong is most accurate at an integral distance of 80-100 km for CMAQ and TROPOMI, and 100-120 km for OMI. Before 60 km, the fitted emission in the three plume is close to each other and have a similar trend on integral distance as the true emission. However, the fitted emission turns flat after 140 km.

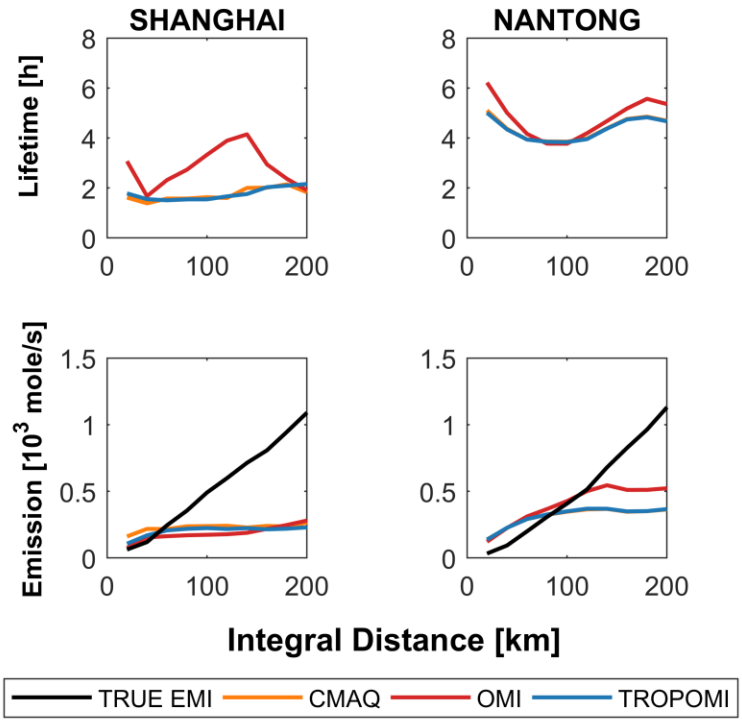

Figure 4.10 The correlation of EMG fitting result of the lifetime and the total emission to integral distance for Shanghai and Nantong under windy condition

4.3.3 Uncertainties

The uncertainty of the EMG fitting process has been well established in previous researches (Beirle et al., 2011; Lu et al., 2015). Here we would like to discuss the uncertainty due to the filters on the satellite pixels and the integral range. Filters are often applied to the satellite pixels to reduce the uncertainties (Zhao and Wang., 2009; Tang et al., 2013). We filter the pixels if they have no available NO_2 data from the satellite or if they locate in the outer 5 bands in both satellites, and we use these filtered grids to resample the ideal plume. Although the total number of satellite pixels in the research region drops 73% and 25% for OMI and TROPOMI separately, the resampled results do not show visible differences, and the EMG fitting results are almost the same. The results show that

the filters on the satellite pixels only contribute limited uncertainty to the estimated emissions.

In previous research, the impact of the integral range on the fitted emission has been estimated as 10% (Beirle et al., 2011; Liu, F. et al., 2016). In this study, however, the fitted emission has a much higher dependence on the integral distance. For example, the method totally fails for Shanghai after an integral distance of 100 km under calm wind condition, and 40 km under windy condition, as the fitted emission remains the same level and the true emission is growing with distance. For Nantong, the integral distance has to reach 160 km for an accurate estimation under calm wind condition, and under windy condition, the integral distance should be below 120 km for accurate estimation. The results indicate that the integral distance plays an important role in EMG fitting, and when applying the EMG fitting, the effect of integral distance should be considered.

4.4 Conclusions

We investigate the uncertainties in applying the EMG fitting of satellite NO_2 observations to derive city-scale NO_X emissions. We use two synthetic datasets: An idealized Gaussian plume and the 4-km CMAQ simulation results for the summer over the YRD region. Sampling pixels equivalent to OMI and TROPOMI were tested compared to the original 4-km CMAQ results. The TROPOMI resolution is sufficiently high that the synthetic dataset resampled using TROPOMI pixels yield essentially the same results as the original CMAQ data. In comparison, the effect of the low resolution of OMI resampling than TROPOMI become clear using the idealized Gaussian plume dataset. Given the orientation wind, the low bias is > 22% for westly wind due mostly to a 30% overestimate

of NO_X. The low emission estimate bias for southerly wind is reduced to > 7% because of the higher OMI sampling resolution in the N-S than E-W direction.

For the idealized Gaussian plume, the cross-section integral distance is known, and a shorter integral distance introduces low biases in emission estimates. In the applications of using satellite measurements, the cross-section integral distance is not known. When using the CMAQ simulations, the total NO_X emission increases with the selected cross-section integral distance. While the EMG fitting method derived NO_X emission also increases with cross-section integral distance at first, the increasing rate is deficient after a certain cross-section integral distance, suggesting that the EMG fitting method is insensitive to relatively low emissions outside the city. It is for the same reason that the EMG fitting method can tolerate some transgression of low-level outflow from another city like in the case of Shanghai. Based on the two city cases we studied, we suggest using a range of integral distance from 40 to 200 km and find the maximum NO_X emission estimate as the optimal value when the integral distance is not known.

Unlike the idealized Gaussian plume case, we only found some evidence of a low estimate bias due to the coarse-resolution sampling of OMI (in Shanghai) when using CMAQ results. The deviation from the Gaussian plume assumption and the emission dependence on the cross-section integral distance could mask out this bias. The former factor is also reflected in that a city-cluster type emission source like Nantong is not a point or Gaussian-shaped source as assumed in the EMG fitting method. Overall, our analysis shows that the EMG fitting method can be applied to OMI and TROPOMI observations to examine city-scale emission trends although factors such as the size of the city emission,

deviation from the Gaussian plume assumption, the emission dependence on the cross-section integral distance, and background interference need to be investigated.

CHAPTER 5. CONCLUSIONS AND FUTURE WORK

5.1 Ozone observation derived constraints

In CHAPTER 1, we extend the sensitivities of the ozone-precursor relationship from ozone concentrations to peak time. We find that the sensitivities of ozone peak time and concentration are complimentary for regions with large anthropogenic emissions such as China. Currently, the empirical kinetic modeling approach (EKMA) diagram (for ozone concentrations) is being used extensively in many metropolitan environmental protection organizations in China to justify the strategies to control NO_X or VOC emissions. Adding ozone peak time sensitivities will enable more information extraction from available regulatory monitoring data. More importantly, it improves the assessment of model biases, such as in the emission inventories of NO_X and VOCs. These biases in model simulations can lead to erroneous emission control strategies and need to be corrected before air quality models can be used in policy applications. The extension of the EKMA diagram to ozone peak time also applies to other regions of the world where anthropogenic emissions dominate ozone production.

In CHAPTER 1, we also identify that the nocturnal boundary layer height is underestimated. Figure 5.1 shows the simulated nocturnal boundary layer height compared to other researches. The underestimation of the nocturnal mixing strength results in an accumulation of the NO_X emission in the shallow boundary layer, and the nighttime surface ozone in the model is depleted through titration effect. With enhanced mixing added, the model is able to reproduce the observed nocturnal ozone concentrations, indicating that the

nighttime mixing height should be increased to at least 100 m for the SW region, 200m for the NW, NE, and PRD regions, and 500m for NCP and YRD region.

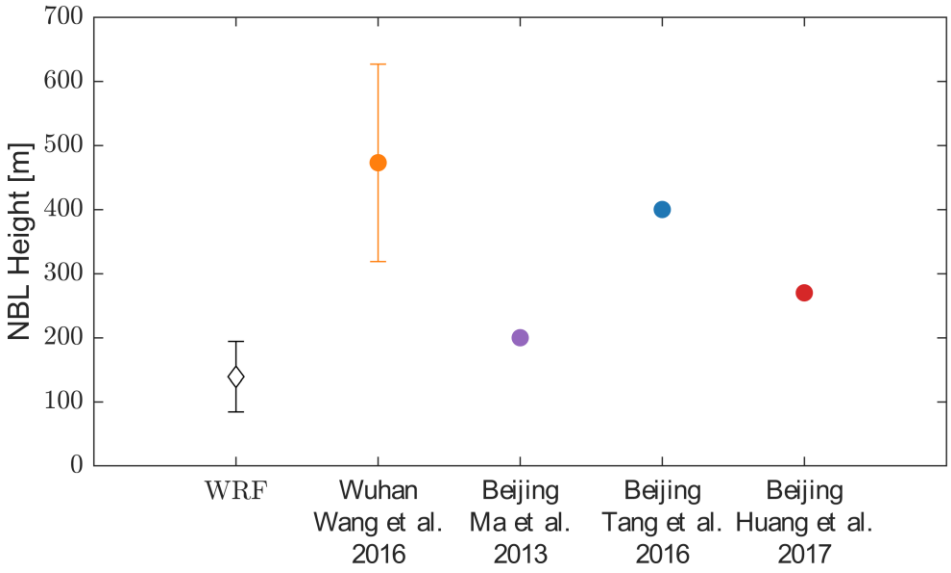

Figure 5.1 Nocturnal boundary layer height from WRF simulation and from observations in other literatures

The future work of the research involves extending the ozone peak time constraints to biogenic emission dominated regions and validating the relationships using local measurements. Li et al., (2019) have applied the ozone peak time and peak concentration relationships in the continental U.S. and suggest an underestimation of the soil NO_X emission in the south, and find overestimations of the isoprene emissions in central, south, and southwest consistent with results from the OMI HCHO column analysis.

5.2 Impact of OVOC and RO_2 on ozone production

In CHAPTER 2, we identified that the intermedia OVOCs produced from the oxidation of RH are a critical source of RO_2, which promotes the production of ozone and accelerate the atmospheric oxidation process as a positive feedback. The modeling analysis constrained by in situ measurements from Wangdu campaign in China indicates a large underestimation of the OVOC and PAN production from hydrocarbons in the simplified mechanism. The underestimated OVOC level consequently lead to an underestimation of the HO_2 and RO_2 production, and a lower ozone production rate. We also find that the lack of the OVOCs in the simplified mechanism leads to underestimated ozone production sensitivity to the NO_X emission, and thus the current 3-D model using the simplified mechanism may have biased results.

The future work of this study involves developing a new photochemistry mechanism to correct the OVOC and RO_2 production from the hydrocarbons. The new mechanism can be based on existing simplified mechanism by adding critical reactions or based on the MCM mechanism by reducing the unimportant reactions. The mechanism development will require a thorough understanding of the radical cycle, and we investigate the radical cycle rates in Wangdu in Figure 5.2 and Figure 5.3. However, the mechanism should satisfy varying chemistry conditions, and additional analysis of the radical cycle should be conducted by in situ observations under other chemical and meteorology conditions.

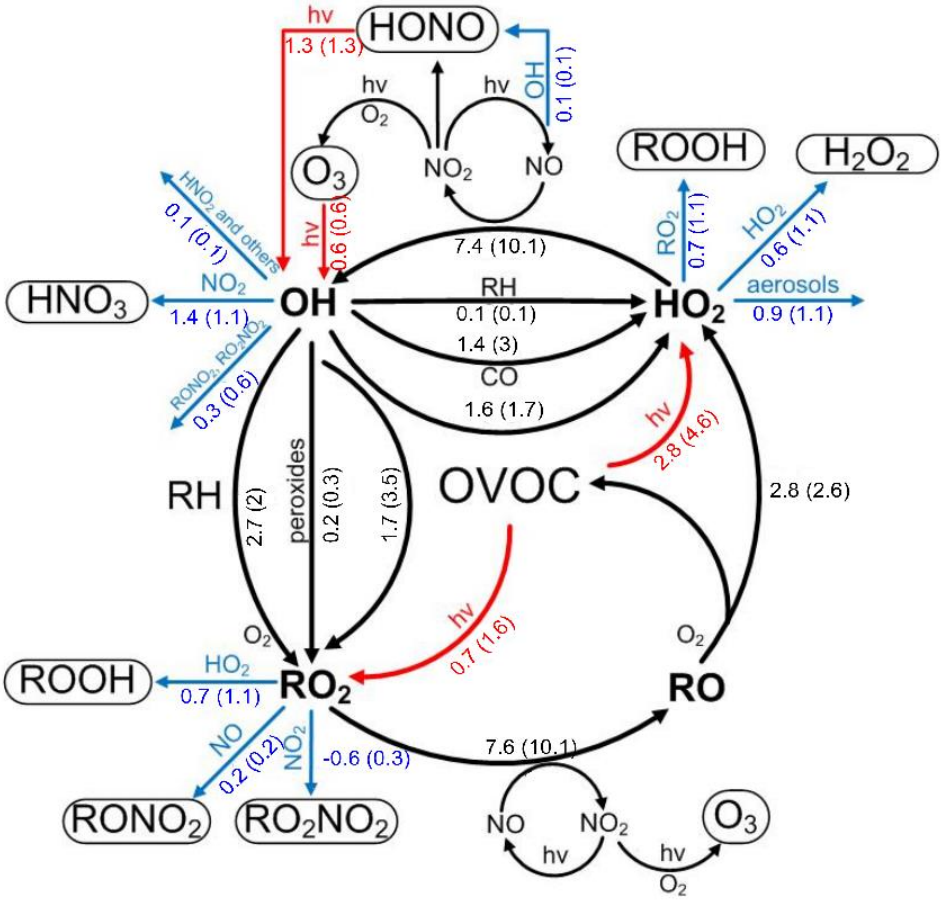

Figure 5.2 Daytime averaged (6 AM to 6 PM) radical cycle rates [ppbv/h] for Wangdu data using MCM mechanism. The number outside the bracket shows the value in the boundary layer of the 1-D model. The number inside the bracket shows the value in the box model.

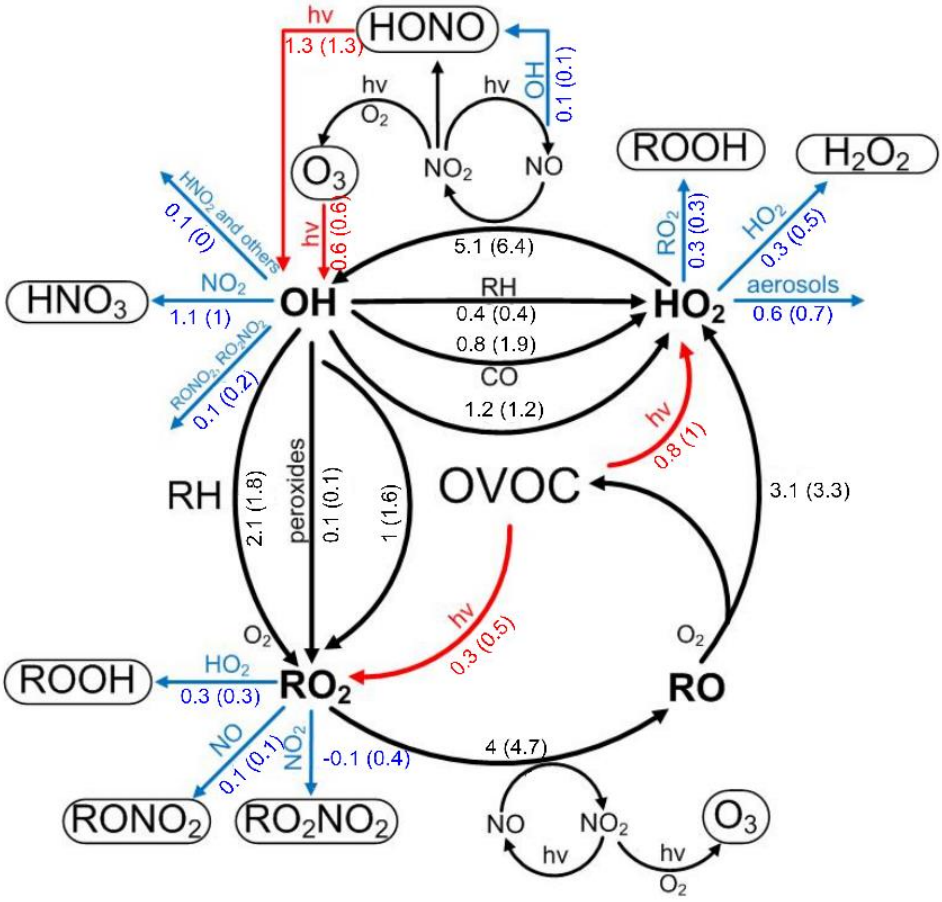

Figure 5.3 Same as Figure 5.2 but for GCM mechanism.

5.3 Effect of cross-section integral distance on EMG fitting

In CHAPTER 4, we show that the cross-section integral distance can dominate the error in EMG fitting of NO_X emissions from satellite observed NO_2 columns using both idealized plumes and CMAQ simulated plumes in the Yangtze River Delta region. The idealized plume suggest that the accuracy is better under longer integral distance, however, in the CMAQ simulated plumes, longer integral distance leads to worse results. In Shanghai and Nantong under calm wind condition, the fitted NO_X emission increases with the cross-section integral distance, however, the increasing rate drops dramatically after the cross-section integral distance reaches a certain value, indicating that the EMG fitting is

insensitive to relatively low emissions. As the true emission continues to increase with the distance, the bias of the fitted emission can be large. In the application of the EMG fitting, the cross-section integral distance often uses empirical values ranging from 180 km to 300 km, and the uncertainty due to the cross-section integral distance is estimated for 10% (Beirle et al., 2011; Fioletov et al., 2015; Goldberg et al., 2019; Liu, F. et al., 2016). With point sources without other sources at a close range, the "visual inspection" method may work, however, for regions with complex source distribution such as China, a determined method is necessary, and the corresponding uncertainty should be analyzed.

The future work of this study involves developing a method for selecting the proper cross-section integral distance with the EMG fitting. Based on the current results for Shanghai and Nantong, the proper distance should be correlated to the increasing rate of the fitted emissions with respect to the cross-section integral distance. After the method is developed, the uncertainty can be determined by applying the method on simulated NO_2 plumes similar to this research, and the uncertainty is expected to be much larger than current 10%.

APPENDIX A. DESCRIPTION OF DEFAULT SUBHEADING SCHEME

A.1 Atmospheric chlorine chemistry

Chlorine atoms (Cl) are known for the destruction of ozone in the stratosphere and the troposphere (Seinfeld et al., 2016). However, in polluted regions, Cl can initiate the oxidation of VOCs and produce RO_2 radicals and hydrochloric acid (HCl), promoting ozone production (R A.1).

$$RH + Cl + O_2 \rightarrow RO_2 + HCl \qquad \text{(R A.1)}$$

The Cl atoms react with RH and OVOCs with a much faster rate than OH (Figure A.1). However, unlike the OH radical, the Cl atoms cannot regenerate from the oxidation process of VOCs. The global average of the tropospheric Cl concentration is ~10^4 molecules cm^{-3} (Saiz-Lopez & Glasow, 2012), much lower than the global average of tropospheric OH of ~10^6 molecules cm^{-3} (Liang et al., 2017). Despite the low abundance of the Cl atoms in the troposphere, Cl atoms contribute ~3% to the total oxidation of CH4, and regionally the percentage can reach as high as 20% (Hossaini et al., 2016).

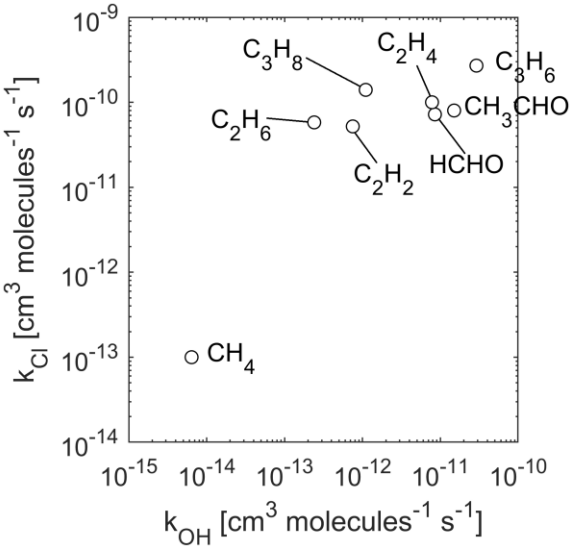

Figure A.1 Kinetic rates for several hydrocarbons and aldehydes with OH radicals and Cl atoms.

The major sources of Cl atoms in the daytime include the rapid photolysis of nitryl chloride ($ClNO_2$) and molecular chlorine (Cl_2), and also the reaction between OH and HCl (R A.2-R A.4).

$$ClNO_2 + h\nu \rightarrow Cl + NO_2 \quad \text{(R A.2)}$$

$$Cl_2 + h\nu \rightarrow 2Cl \quad \text{(R A.3)}$$

$$OH + HCl_{(g)} \rightarrow Cl + H_2O \quad \text{(R A.4)}$$

The $ClNO_2$ is produced by the aerosol uptake of N_2O_5 during the night (R A.5), as the N_2O_5 has a deficient daytime concentration due to the heat decomposition into NO_2 and NO_3, and NO_3 has a very short lifetime of seconds during the day due to photolysis (Brown & Stutz, 2012; Faxon & Allen, 2013). The production of $ClNO_2$ from the uptake of N_2O_5 competes with the hydrolysis of N_2O_5 (R A.6), and the observation derived yield of $ClNO_2$

from the N_2O_5 uptake can vary between 1%-104% in China, with maximum $ClNO_2$ concentrations over 2 ppbv (Liu X. et al., 2017; Wang, T. et al., 2016; Tham et al., 2018).

$$N_2O_5 + Cl^-_{(l)} \rightarrow ClNO_2 + NO_3^- \quad \text{(R A.5)}$$

$$N_2O_5 + H_2O_{(l)} \rightarrow 2HNO_3 \quad \text{(R A.6)}$$

The Cl_2 can be generated from aerosol uptake of hypochlorous acid (HOCl) and chlorine nitrate ($ClONO_2$) (R A.7-R A.11), activating chlorine ions in the aerosol (Vogt et al., 1996).

$$Cl + O_3 \rightarrow ClO + O_2 \quad \text{(R A.7)}$$

$$ClO + HO_2 \rightarrow HOCl + O_2 \quad \text{(R A.8)}$$

$$ClO + NO_2 + (M) \rightarrow ClONO_2 + (M) \quad \text{(R A.9)}$$

$$HOCl + Cl^- + H^+ \rightarrow Cl_2 + H_2O \quad \text{(R A.10)}$$

$$ClONO_2 + Cl^- \rightarrow Cl_2 + NO_3^- \quad \text{(R A.11)}$$

Other mechanisms that produce Cl_2 involve the surface reaction of OH and Cl^- and the uptake of $ClNO_2$ in high acidic aerosols (Knipping et al., 2000; Roberts et al., 2008). The new mechanisms are based on experimental studies and have not been validated through observations.

A.2 Additional reactions in the mechanism

We expand the previous REAM mechanism with 9 chlorine species including chlorine atoms (Cl), chlorine monoxide (ClO), chlorine dioxide (OClO), hydrochloric acid (HCl), hypochlorous acid (HOCl), molecular chlorine (Cl_2), nitryl chloride ($ClNO_2$), chlorine nitrite (ClONO), and chlorine nitrate ($ClONO_2$). The extended mechanism contains 22 inorganic reactions, 22 organic reactions, 7 photolysis reactions, and 3 heterogeneous reactions. The names of the organic species in REAM are listed in Table A.1 and the reactions are listed in Table A.2. The products in the chlorine-organic reactions use the same product as OH-organic reactions replacing H_2O formation with HCl.

Table A.1 Tracer names in REAM and the corresponding species

REAM tracer name	Species
CH4	Methane
MP	Methyl hydroperoxide
CH2O	Formaldehyde
HCOOH	Formic acid
MOH	Methanol
ALD2	Acetaldehyde
C2H6	Ethane
C3H8	Propane
ALK4	Alkanes with equal or more than 4 carbons
R4N2	Organic nitrites with more than 4 carbons
ACTA	Acetic acid
RCHO	Aldehydes with equal or more than 3 carbons
ACET	Acetone
MEK	Methyl ethyl ketone
EOH	Ethanol
ROH	Alcohols with equal or more than 3 carbons
PRPE	Alkenes with equal or more than 3 carbons
C2H4	Ethene
C2H2	Acetylene
ISOP	Isoprene
TOL	Aromatics with k(OH) < 1×10^{-11} cm^3 $molecule^{-1}$ s^{-1}
XYL	Aromatics with k(OH) > 1×10^{-11} cm^3 $molecule^{-1}$ s^{-1}

Table A.2 The chlorine related reactions added to REAM mechanism

Inorganic reactions	**Rate constant at 298K, 1 atm [cm^3 $molecule^{-1}$ s^{-1}]**	**reference**
$Cl+O_3 \rightarrow ClO+O_2$	1.21E-11	Atkinson et al., 2007
$Cl+H_2 \rightarrow HCl+H$	1.68E-14	Atkinson et al., 2007
$ClO+NO \rightarrow Cl+NO_2$	1.67E-11	Atkinson et al., 2007
$ClO+HO_2 \rightarrow HOCl+O_2$	6.88E-12	Atkinson et al., 2007
$ClO+NO_2+M \rightarrow ClONO_2+M$	2.17E-12	Atkinson et al., 2007
$ClO+ClO \rightarrow Cl_2+O_2$	4.82E-15	Atkinson et al., 2007
$ClO+ClO \rightarrow OClO+Cl$	3.53E-15	Atkinson et al., 2007
$ClO+ClO \rightarrow 2Cl+O_2$	8.06E-15	Atkinson et al., 2007
$Cl_2+OH \rightarrow HOCl+Cl$	6.48E-14	Atkinson et al., 2007
$ClNO_2+OH \rightarrow HOCl+NO_2$	3.62E-14	Atkinson et al., 2007
$Cl+NO_2+M \rightarrow ClNO_2+M$	3.6E-12	Burkholder et al., 2015
$Cl+NO_2+M \rightarrow ClONO+M$	1.63E-11	Burkholder et al., 2015
$Cl+H_2O_2 \rightarrow HO_2+HCl$	4.10E-13	Atkinson et al., 2007
$HCl+OH \rightarrow Cl+H_2O$	7.86E-13	Burkholder et al., 2015
$Cl+HO_2 \rightarrow HCl+O_2$	3.18E-11	Burkholder et al., 2015
$Cl+HO_2 \rightarrow OH+ClO$	9.06E-12	Burkholder et al., 2015
$ClO+OH \rightarrow HCl+O_2$	1.30E-12	Burkholder et al., 2015
$ClO+OH \rightarrow HO_2+Cl$	1.83E-11	Burkholder et al., 2015
$HOCl+OH \rightarrow ClO+H_2O$	5.60E-13	Burkholder et al., 2015
$Cl+ClONO_2 \rightarrow Cl_2+NO_3$	1.01E-11	Burkholder et al., 2015
$ClONO_2+OH \rightarrow Cl+HO_2+NO_2$	3.97E-13	Burkholder et al., 2015
$ClONO_2+M \rightarrow ClO+NO_2+M$	5.57E-04 (s^{-1})	Zhu & Lin, 2005
Organic reactions	**Rate constant at 298K, 1 atm [cm^3 $molecule^{-1}$ s^{-1}]**	**reference**
Cl+CH4 → products	1.03E-13	Atkinson et al., 2006
Cl+MP → products	5.90E-11	Atkinson et al., 2006
Cl+CH2O → products	7.23E-11	Atkinson et al., 2006
Cl+HCOOH → products	1.90E-13	Atkinson et al., 2006
Cl+MOH → products	1.90E-13	Atkinson et al., 2006
Cl+ALD2 → products	8.00E-11	Atkinson et al., 2006
Cl+C2H6 → products	5.76E-11	Atkinson et al., 2006
Cl+C3H8 → products	1.38E-10	Atkinson et al., 2006
Cl+ALK4 → products	2.05E-10	Atkinson et al., 2006
Cl+R4N2 → products	8.50E-11	Atkinson et al., 2006
Cl+ACTA → products	2.65E-14	Atkinson et al., 2006
Cl+RCHO → products	1.30E-10	Atkinson et al., 2006
Cl+ACET → products	2.07E-12	Atkinson et al., 2006
Cl+MEK → products	4.00E-11	Atkinson et al., 2006
Cl+EOH → products	1.01E-10	Atkinson et al., 2006

Cl+ROH→products	1.57E-10	Atkinson et al., 2006
Cl+PRPE→products	2.70E-10	Atkinson et al., 2006
Cl+C2H4→products	1.58E-10	Atkinson et al., 2006
Cl+C2H2→products	5.24E-11	Atkinson et al., 2006
Cl+ISOP→products	4.07E-10	Atkinson et al., 2006
Cl+TOL→products	5.90E-11	Shi & Bernhard, 1999
Cl+XYL→products	1.50E-10	Shi & Bernhard, 1999
Photolysis reactions	**Average noon rates [s^{-1}]**	**reference**
$ClO \rightarrow Cl+O_3$	1.58E-05	Atkinson et al., 2007
$HOCl \rightarrow OH+Cl$	1.42E-04	Atkinson et al., 2007
$OClO \rightarrow O_3+ClO$	5.16E-02	Atkinson et al., 2007
$ClONO_2 \rightarrow Cl+NO_3$	2.87E-05	Atkinson et al., 2007
$ClONO \rightarrow Cl+NO_2$	2.57E-03	Atkinson et al., 2007
$Cl_2 \rightarrow 2Cl$	1.40E-03	Atkinson et al., 2007
$ClNO_2 \rightarrow Cl+NO_2$	2.81E-04	Atkinson et al., 2007
Heterogeneous reactions	**Uptake coefficient (γ)**	**reference**
$N_2O_5+HCl \rightarrow \varphi ClNO_2+(2-\varphi)HNO_3$	0.1	Ammann et al., 2013
$ClONO_2+HCl \rightarrow Cl_2+HNO_3$	0.03	Ammann et al., 2013
$HOCl+HCl \rightarrow Cl_2+H_2O$	0.01	Ammann et al., 2013

We have applied the box model assembled with the extended REAM mechanism to analyze the chlorine chemistry in Wangdu. Figure A.2 shows the comparison of the daytime averaged (6AM to 6 PM) radical concentrations simulated by the box model before and after the chlorine chemistry is added. The OH, HO_2, and RO_2 concentrations rise by 5%, 14% and 22% separately. The corresponding ozone production rate increased by 20% in the daytime. The chlorine atoms also contribute to the oxidation of 16% to methane, 55% to non-methane alkanes, 13% to alkenes, 7% to aromatics, and 5% to isoprene. More details can be found in Liu, X. et al., (2017).

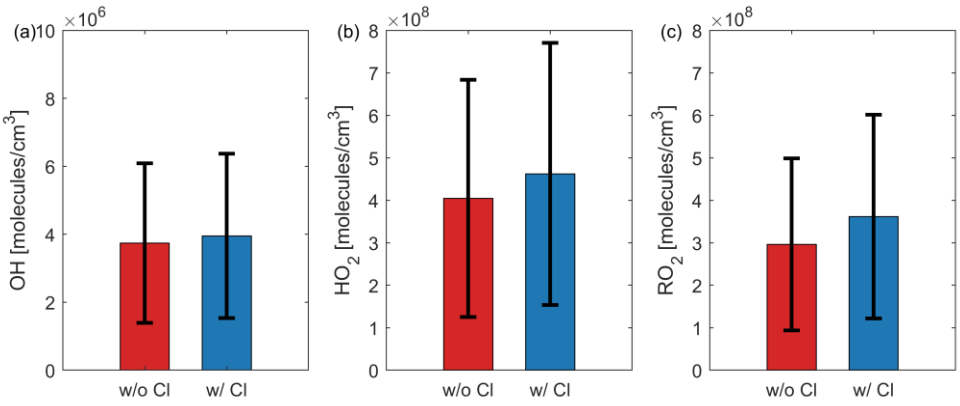

Figure A.2 The effect on daytime (6AM to 6PM) radical concentrations due to the chlorine chemistry

In MCM, the inorganic reactions, photolysis reactions, and heterogeneous reactions are the same as in the REAM mechanism. For the organic reactions of non-lumped species in Table A.2, we directly add those reactions in MCM. For the other species, we only add the reactions with reliable kinetic rates and assume the branching ratio of the products is the same as OH radicals. The organic reactions in MCM are listed in Table A.3. The complex products use the same product as their reactions with OH radical by replacing the H_2O production with HCl.

Table A.3 Additional chlorine related organic reactions in MCM

Organic reactions	Rate constant at 298K, 1 atm [cm^3 $molecule^{-1}$ s^{-1}]	**reference**
$Cl+CH_4 \rightarrow CH_3+HCl$	1.03E-13	Atkinson et al., 2006
$Cl+C_2H_2 \rightarrow$products	5.24E-11	Atkinson et al., 2006
$Cl+C_2H_4 \rightarrow$ products	1.58E-10	Atkinson et al., 2006
$Cl+C_2H_6 \rightarrow C_2H_5+HCl$	5.76E-11	Atkinson et al., 2006
$Cl+C_3H_6 \rightarrow$products	2.70E-10	Atkinson et al., 2006
$Cl+C_3H_8 \rightarrow C_3H_7+HCl$	1.38E-10	Atkinson et al., 2006
$Cl+n\text{-}C_4H_{10} \rightarrow C_4H_9+HCl$	2.05E-10	Atkinson et al., 2006
$Cl+HCHO \rightarrow HCl+HCO$	7.23E-11	Atkinson et al., 2006
$Cl+CH_3CHO \rightarrow HCl+CH_3CO$	8.00E-11	Atkinson et al., 2006
$Cl+CH_3C(O)CH_3 \rightarrow$products	2.07E-12	Atkinson et al., 2006
$Cl+CH_3C(O)C_2H_5 \rightarrow$products	3.60E-11	Atkinson et al., 2006

$Cl+CH_3OH \rightarrow products$	5.50E-11	Atkinson et al., 2006
$Cl+C_2H_5OH \rightarrow products$	1.01E-10	Atkinson et al., 2006
$Cl+CH_3OOH \rightarrow products$	5.90E-11	Atkinson et al., 2006
$Cl+HCOOH \rightarrow products$	1.90E-13	Atkinson et al., 2006
$Cl+CH_3COOH \rightarrow products$	2.65E-14	Atkinson et al., 2006
$Cl+CH_3ONO_2 \rightarrow products$	2.40E-13	Atkinson et al., 2006
$Cl+C_2H_5ONO_2 \rightarrow products$	4.70E-12	Atkinson et al., 2006
$Cl+n\text{-}C_3H_7ONO_2 \rightarrow products$	2.20E-11	Atkinson et al., 2006
$Cl+i\text{-}C_3H_7ONO_2 \rightarrow products$	3.80E-12	Atkinson et al., 2006
$Cl+ISOP \rightarrow products$	4.07E-10	Atkinson et al., 2006
$Cl+TOL \rightarrow products$	5.90E-11	Shi et al., 1997
$Cl+XYL \rightarrow products$	1.50E-10	Shi et al., 1997

REFERENCES

Ashok, A. and Barrett, S. R. H.: Adjoint-based computation of U.S. nationwide ozone exposure isopleths, Atmos. Environ., 133, 68-80, 2016.

Ammann, M. et al.: Evaluated kinetic and photochemical data for atmospheric chemistry: Volume VI – heterogeneous reactions with liquid substrates, Atmos. Chem. Phys., 13, 8045–8228, 2013.

Atkinson, R. et al.: Evaluated kinetic and photochemical data for atmospheric chemistry: Volume I - gas phase reactions of Ox, HOx, NOx and SOx species, Atmos. Chem. Phys., 4, 1461-1738, 2004.

Atkinson, R. et al.: Evaluated kinetic and photochemical data for atmospheric chemistry: Volume II – gas phase reactions of organic species, Atmos. Chem. Phys., 6, 3625-4055, 2006.

Atkinson, R. et al.: Evaluated kinetic and photochemical data for atmospheric chemistry: Volume III – gas phase reactions of inorganic halogens, Atmos. Chem. Phys., 7, 981-1191, 2007.

Beirle, S. et al.: Estimate of nitrogen oxide emissions from shipping by satellite remote sensing, Geophys. Res. Lett., 31, L18102, 2004.

Beirle, S. et al.: Megacity emissions and lifetimes of nitrogen oxides probed from space, Science, 333, 1737-1739, 2011.

Bey, I. et al.: Global modeling of tropospheric chemistry with assimilated meteorology: Model description and evaluation, J. Geophys. Res.-Atmos., 106, 23073-23095, 2001.

Blanchard, C. L. and Fairley, D.: Spatial mapping of VOC and NOx-limitation of ozone formation in central California, Atmos. Environ., 35, 3861-3873, 2001.

Bloss, C. et al.: Development of a detailed chemical mechanism (MCMv3.1) for the atmospheric oxidation of aromatic hydrocarbons, Atmos. Chem. Phys., 5, 641-664, 2005.

Boersma, K. F. et al.: An improved tropospheric NO2 column retrieval algorithm for the Ozone Monitoring Instrument, Atmos. Meas. Tech., 4, 1905-1928, 2011.

Bohn, B. et al.: Photolysis frequency measurement techniques: results of a comparison within the ACCENT project, Atmos. Chem. Phys., 8, 5373–5391, 2008.

Brown, S. S. and Stutz, J.: Nighttime radical observations and chemistry, Chem. Soc. Rev., 41, 6405-6447, 2012.

Brunekreef B. and Holgate S. T.: Air pollution and health, Lancet, 360, 1233-1242, 2002.

Burkholder et al.: Chemical Kinetics and Photochemical Data for Use in Atmospheric Studies, Evaluation No. 18. JPLPublication 15-10, Jet Propulsion Laboratory: Pasadena, CA, 2015.

CNEMC: Monthly Report on Air Quality of China cities. China National Environmental Monitoring Centre, http://www.cnemc.cn/jcbg/kqzlzkbg/201808/P020181010529659662339.pdf (in Chinese), 2018.

de Foy, B. et al.: Model evaluation of methods for estimating surface emissions and chemical lifetimes from satellite data, Atmos. Environ., 98, 66-77, 2014.

de Foy, B. et al.: Estimates of power plant NOx emissions and lifetimes from OMI NO2 satellite retrievals, Atmos. Environ., 116, 1-11, 2015.

Ding D. et al.: Impacts of emissions and meteorological changes on China's ozone pollution in the warm seasons of 2013 and 2017, Front. Env. Sci. Eng., 13, 76, 2019.

Duncan, B. N. et al.: A space-based, high-resolution view of notable changes in urban NOx pollution around the world (2005-2014), J. Geophys. Res. Atmos., 121, 976-996, 2016.

Faxon, C. B. and Allen, D. T.: Chlorine chemistry in urban atmospheres: a review, Environ. Chem., 10, 221-233, 2013.

Fioletov, V. E. et al.: Lifetimes and emissions of SO2 from point sources estimated from OMI, Geophys. Res. Lett., 42, 1969-1976, 2015.

Fischer, E. V. et al.: Atmospheric peroxyacetyl nitrate (PAN): a global budget and source attribution, Atmos. Chem. Phys., 14, 2679-2698, 2014.

Fu, T. M. et al.: Global budgets of atmospheric glyoxal and methylglyoxal, and implications for formation of secondary organic aerosols, J. Geophys. Res., 113, D15303, 2008.

Fuchs, H. et al.: OH reactivity at a rural site (Wangdu) in the North China Plain: contributions from OH reactants and experimental OH budget, Atmos. Chem. Phys., 17, 645-661, 2017.

Gao, W. et al.: Long-term trend of O3 in a mega City (Shanghai), China: Characteristics, causes, and interactions with precursors, Sci. Total Environ., 603-604, 425-433, 2017.

Geng, F. et al.: Characterization of ozone, NOx, and VOCs measured in Shanghai, China, Atmos. Environ., 42, 6873-6883, 2008.

Goldberg, D. L. et al.: A top-down assessment using OMI NO2 suggests an underestimate in the NOx emissions inventory in Seoul, South Korea, during KORUS-AQ, Atmos. Chem. Phys., 19, 1801-1818, 2019.

Griffith, S. M. et al.: Measurements of hydroxyl and hydroperoxyl radicals during CalNex-LA: Model comparisons and radical budgets, J. Geophys. Res. Atmos., 121, 4211-4232, 2016.

Gu, D. et al.: Reduction in NOx emission trends over China: Regional and seasonal variations, Environ. Sci. Tech., 47, 12912-12919, 2013.

Gu, D. et al.: Anthropogenic emissions of NOx over China: Reconciling the difference of inverse modeling results using GOME-2 and OMI measurements, J. Geophys. Res. Atmos., 119, 2014JD021644, 2014.

Gu, D. et al.: Inverse modeling of NOx emissions over eastern China: Uncertainties in photochemical nonlinearity, Atmos. Meas. Tech., 9, 5193-5201, 2016.

Guenther, A. B. et al.: The Model of Emissions of Gases and Aerosols from Nature version 2.1 (MEGAN2.1): an extended and updated framework for modeling biogenic emissions, Geosci. Model Dev., 5, 1471-1492, 2012.

Guo, H. et al.: Simulation of summer ozone and its sensitivity to emission changes in China, Atmos. Pollut. Res., 10, 1543-1552, 2019.

Hazra, M. K. et al.: Hydrolysis of glyoxal in water-restricted environments: formation of organic aerosol precursors through formic acid catalysis, J. Phys. Chem. A, 118, 4095-4105, 2014.

Hossaini, R. et al.: A global model of tropospheric chlorine chemistry: Organic versus inorganic sources and impact on methane oxidation, J. Geophys. Res. Atmos., 121, 14271-14297, 2016.

Hu, X. et al.: Evaluation of Three Planetary Boundary Layer Schemes in the WRF Model, J. Appl. Meteorol. Clim., 49, 1831-1844, 2010.

Hu, L. et al.: Global budget of tropospheric ozone: Evaluating recent model advances with satellite (OMI), aircraft (IAGOS), and ozonesonde observations, Atmos. Environ., 167, 323-334, 2017.

Huang, C. et al.: Emission inventory of anthropogenic air pollutants and VOC species in the Yangtze River Delta region, China, Atmos. Chem. Phys., 11, 4105-4120, 2011.

Huang, M. et al.: Estimate of Boundary-Layer Depth Over Beijing, China, Using Doppler Lidar Data During SURF-2015, Bound.-Lay. Meteorol., 162, 503-522, 2017.

Jenkin, M. E. et al.: The tropospheric degradation of volatile organic compounds: a protocol for mechanism development, Atmos. Environ., 31, 81-104, 1997.

Jenkin, M. E. et al.: Protocol for the development of the Master Chemical Mechanism, MCM v3 (Part B): tropospheric degradation of aromatic volatile organic compounds, Atmos. Chem. Phys., 3, 181-193, 2003.

Jenkin, M. E. et al.: Development and chamber evaluation of the MCM v3.2 degradation scheme for β-caryophyllene, Atmos. Chem. Phys., 12, 5275-5308, 2012.

Jenkin, M. E. et al.: The MCM v3.3.1 degradation scheme for isoprene, Atmos. Chem. Phys., 15, 11433-11459, 2015.

Jimenez, P. and Baldasano, J. M.: Ozone response to precursor controls in very complex terrains: Use of photochemical indicators to assess O3-NOx-VOC sensitivity in the northeastern Iberian Peninsula, J. Geophys. Res., 109, D20309, 2019.

Jin. X. and Holloway T.: Spatial and temporal variability of ozone sensitivity over China observed from the Ozone Monitoring Instrument, J. Geophys. Res. Atmos., 120, 7229-7246, 2015.

Karl, T. et al.: Urban flux measurements reveal a large pool of oxygenated volatile organic compound emissions, Proc. Natl. Acad. Sci., 115, 1186-1191, 2018.

Kinosian, J. R.: Ozone-Precursor Relationships from EKMA Diagrams, Environ. Sci. Technol., 16, 880-883, 1982.

Kleinman, L. I. et al.: Ozone production rate and hydrocarbon reactivity in 5 urban areas: A cause of high ozone concentration in Houston, Geophys. Res. Lett., 29, 105-1-105-4, 2002.

Knipping, E. M. et al.: Experiments and Simulations of Ion-Enhanced Interfacial Chemistry on Aqueous NaCl Aerosols, Science, 288, 301-306, 2000.

Kokkola, H. et al.: The role of low volatile organics on secondary organic aerosol formation, Atmos. Chem. Phys., 14, 1689-1700, 2014.

Kong, H. et al.: High-resolution (0.05° × 0.05°) NOx emissions in the Yangtze River Delta inferred from OMI, Atmos. Chem. Phys., 19, 12835-12856, 2019.

Lamsal, L. N. et al.: Ground-level nitrogen dioxide concentrations inferred from the satellite-borne Ozone Monitoring Instrument, J. Geophys. Res., 113, D16308, 2008.

Lamsal, L. N. et al.: U.S. NO2 trends (2005-2013): EPA Air Quality System (AQS) data versus improved observations from the Ozone Monitoring Instrument (OMI), Atmos. Environ., 110, 130-143, 2015.

Laughner, J. L. et al.: Effects of daily meteorology on the interpretation of space-based remote sensing of NO2, Atmos. Chem. Phys., 16, 15247-15264, 2016.

Lee, Y. N. et al.: Atmospheric carbonyl compounds at a rural southeastern United States site, J. Geophys. Res., 100, 25933-25944, 1995.

Lee, G. et al.: Variations of regional background peroxyacetyl nitrate in marine boundary layer over Baengyeong Island, South Korea, Atmos. Environ., 61, 533-541, 2012.

Li, L. et al.: Air quality and emissions in the Yangtze River Delta, China, Atmos. Chem. Phys., 11, 1621-1639, 2011.

Li, Y. et al.: Importance of NOx control for peak ozone reduction in the Pearl River Delta region, J. Geophys. Res. Atmos., 118, 9428-9443, 2013.

Li, J. et al.: Observational constraints on glyoxal production from isoprene oxidation and its contribution to organic aerosol over the Southeast United States, J. Geophys. Res. Atmos., 121, 9849-9861, 2016.

Li, N. et al.: Impacts of biogenic and anthropogenic emissions on summertime ozone formation in the Guanzhong Basin, China, Atmos. Chem. Phys., 18, 7489-7507, 2018.

Li, K. et al.: Anthropogenic drivers of 2013-2017 trends in summer surface ozone in China, Proc. Natl. Acad. Sci., 116, 422-427, 2019.

Li, J. et al.: Dependence of Summertime Surface Ozone on NOx and VOC Emissions Over the United States: Peak Time and Value, Geophys. Res. Lett., 46, 2018GL081823, 2019.

Liang, Q. et al.: Deriving Global OH Abundance and Atmospheric Lifetimes for Long‐Lived Gases: A Search for CH3CCl3 Alternatives, J. Geophys. Res. Atmos., 122, 11914-11933, 2017.

Lin, J. et al.: Global model simulation of summertime U.S. ozone diurnal cycle and its sensitivity to PBL mixing, spatial resolution, and emissions, Atmos. Environ., 42, 8470-8483, 2008.

Lin, J. and McElroy, M. B.: Impacts of boundary layer mixing on pollutant vertical profiles in the lower troposphere: implications to satellite remote sensing, Atmos. Environ., 44, 1726-1739, 2010.

Lin, J. et al.: Trend and Interannual Variability of Chinese Air Pollution since 2000 in Association with Socioeconomic Development: A Brief Overview, Atmos. Ocean. Sci. Lett., 6, 84-89, 2013.

Liu, Z. et al.: Summertime photochemistry during CAREBeijing-2007: ROX budgets and O3 formation, Atmos. Chem. Phys., 12, 7737-7752, 2012a.

Liu, Z. et al.: Exploring the missing source of glyoxal (CHOCHO) over China, Geophys. Res. Lett., 39, L10812, 2012b.

Liu, Z. et al.: Evidence of Aerosols as a Media for Rapid Daytime HONO Production over China, Environ. Sci. Technol., 48, 14386-14391, 2014.

Liu, F. et al.: NOx lifetimes and emissions of cities and power plants in polluted background estimated by satellite observations, Atmos. Chem. Phys., 16, 5283–5298, 2016.

Liu, Y. et al.: In situ monitoring of atmospheric nitrous acid based on multi-pumping flow system and liquid waveguide capillary cell, J. Environ. Sci., 43, 273-284, 2016.

Liu, F. et al.: NOx emission trends over Chinese cities estimated from OMI observations during 2005 to 2015, Atmos. Chem. Phys., 17, 9261-9275, 2017.

Liu, X. et al.: High levels of daytime molecular chlorine and nitryl chloride at a rural site on the North China Plain, Environ. Sci. Technol., 51, 9588-9595, 2017.

Liu, H. et al.: Ground-level ozone pollution and its health impacts in China, Atmos. Environ., 173, 223-230, 2018.

Liu, Y. et al.: Emissions, Chemical Composition, and Spatial and Temporal Allocation of the BVOCs in the Yangtze River Delta Region in 2014, Environ. Sci., 39, 608-617, 2018.

Lou, S. et al.: Impacts of aerosols on surface-layer ozone concentrations in China through heterogeneous reactions and changes in photolysis rates, Atmos. Environ., 85, 123-138, 2014.

Lu, K. et al.: Missing OH source in a suburban environment near Beijing: observed and modelled OH and HO2 concentrations in summer 2006, Atmos. Chem. Phys., 13, 1057-1080, 2013.

Lu, Z. et al.: Emissions of nitrogen oxides from US urban areas: estimation from Ozone Monitoring Instrument retrievals for 2005-2014, Atmos. Chem. Phys., 15, 10367-10383, 2015.

Lu, X. et al.: Severe surface ozone pollution in China: a global perspective, Environ. Sci. Technol. Lett., 5, 487-494, 2018.

Lu, X. et al.: Exploring 2016-2017 surface ozone pollution over China: source contributions and meteorological influences, Atmos. Chem. Phys., 19, 8339-9361, 2019.

Ma, Z. et al.: Vertical ozone characteristics in urban boundary layer in Beijing, Environ. Monit. Assess., 185, 5449-5460, 2013.

Ma, Z. et al.: Satellite-Based Spatiotemporal Trends in PM2.5 Concentrations: China, 2004-2013, Environ. Health Perspect., 124, 184-192, 2015.

Ma, Z. et al.: Significant increase of surface ozone at a rural site, north of eastern China, Atmos. Chem. Phys., 16, 3969-3977, 2016.

Mellouki, A. et al.: Atmospheric chemistry of oxygenated volatile organic compounds: impacts on air quality and climate, Chem. Rev., 115, 3984-4014, 2015.

Moore, G. E. and Londergan, R. J.: Sampled Monte Carlo uncertainty analysis for photochemical grid models, Atmos. Environ., 35, 4863-4876, 2001.

Parra, M.A. et al.: Ambient air levels of volatile organic compounds (VOC) and nitrogen dioxide (NO2) in a medium-size city in Northern Spain, Atmos. Environ., 407, 999-1009, 2009.

Phillips, G. J. et al.: Peroxyacetyl nitrate (PAN) and peroxyacetic acid (PAA) measurements by iodide chemical ionisation mass spectrometry: first analysis of results in the boreal forest and implications for the measurement of PAN fluxes, Atmos. Chem. Phys., 13, 1129-1139, 2013.

Qian, X. et al.: Characterizing summer and winter carbonyl compounds in Beijing atmosphere, Atmos. Environ., 214, 116845, 2019.

Qu, Z. et al.: Hybrid Mass Balance/4D-Var Joint Inversion of NOx and SO2 Emissions in East Asia, J. Geophys. Res.- Atmos., 124, 8203-8224, 2019.

Ran, L. et al.: Ozone photochemical production in urban Shanghai, China: Analysis based on ground level observations, J. Geophys. Res., 114, D15301, 2009.

Read, K. A. et al.: Multiannual observations of acetone, methanol, and acetaldehyde in remote tropical Atlantic air: implications for atmospheric OVOC budgets and oxidative capacity, Environ. Sci. Technol., 46, 11028-11039, 2012.

Reich, P. B. and Amundson R. G.: Ambient levels of ozone reduce net photosynthesis in tree and crop species, Science, 230, 566-570, 1985.

Ren, X. et al.: Atmospheric oxidation chemistry and ozone production: Results from SHARP 2009 in Houston, Texas, J. Geophys. Res. Atmos., 118, 5770-5780, 2013.

Roberts, J. M.: N2O5 Oxidizes Chloride to Cl2 in Acidic Atmospheric Aerosol, Science, 321, 1059, 2008.

Saha, S. et al.: The NCEP Climate Forecast System Version 2, J. Climate, 27, 2185-2208,2013.

Saiz-Lopez, A. and von Glasow, R.: Reactive halogen chemistry in the troposphere, Chem. Soc. Rev., 41, 6448-6472, 2012.

Saunders, S. M. et al.: Protocol for the development of the Master Chemical Mechanism, MCM v3 (Part A): tropospheric degradation of non-aromatic volatile organic compounds, Atmos. Chem. Phys., 3, 161-180, 2003.

Schlundt, C. et al.: Oxygenated volatile organic carbon in the western Pacific convective center: ocean cycling, air-sea gas exchange and atmospheric transport, Atmos. Chem. Phys., 17, 10837-10854, 2017.

Seinfeld, J. H. and Pandis, S. N.: Atmospheric Chemistry and Physics: From Air Pollution to Climate Change, 3rd, ed., John Wiley & Sons, Inc: New Jersey, 2016.

Shi, J. and Bernhard, M. J.: Kinetic studies of Cl‐atom reactions with selected aromatic compounds using the photochemical reactor‐FTIR spectroscopy technique, Int. J. Chem., 29, 349-358, 1999.

Shim, C. et al.: Source characteristics of oxygenated volatile organic compounds and hydrogen cyanide, J. Geophys. Res., 112, D10305, 2007.

Singh, H. B. et al.: Peroxyacetyl nitrate (PAN) in the unpolluted atmosphere: an important reservoir for nitrogen oxides, Geophys. Res. Lett., 8, 941-944, 1981.

Singh, H. B. et al.: High concentrations and photochemical fate of oxygenated hydrocarbons in the global troposphere, Nature, 378, 50-54, 1995.

Singh, H. B. et al.: Evidence from the Pacific troposphere for large global sources of oxygenated organic compounds, Nature, 410, 1078-1081, 2000.

Singh, H. B. et al.: Analysis of the atmospheric distribution, sources, and sinks of oxygenated volatile organic chemicals based on measurements over the Pacific during TRACE-P, J. Geophys. Res., 109, D15S07, 2004.

Skamarock, W. et al.: A Description of the Advanced Research WRF Version 3, NCAR technical note NCAR/TN-475+STR., 2008.

Tan, Z. et al.: Radical chemistry at a rural site (Wangdu) in the North China Plain: observation and model calculations of OH, HO2 and RO2 radicals, Atmos. Chem. Phys., 17, 663-690, 2017.

Tan, Z. et al.: Exploring ozone pollution in Chengdu, southwestern China: A case study from radical chemistry to O3-VOC-NOx sensitivity, Sci. Total Environ., 636, 775-786, 2018.

Tang, W. et al.: Inverse modeling of Texas NOx emissions using space-based and ground-based NO2 observations, Atmos. Chem. Phys., 13, 11005-11018, 2013.

Tang, G. et al.: Mixing layer height and its implications for air pollution over Beijing, China, Atmos. Chem. Phys., 16, 2459-2475, 2016.

Tham, Y. J. et al.:Heterogeneous N2O5 uptake coefficient and production yield of ClNO2 in polluted northern China: roles of aerosol water content and chemical composition, Atmos. Chem. Phys., 18, 13155-13171, 2018.

Tukey, J. W.: Exploratory Data Analysis, Addison-Wesley, 1977.

U.S. EPA: Integrated Science Assessment for Ozone and Related Photochemical Oxidants, National Center for Environmental Assessment: RTP, NC, EPA/600/R-10/076F, 2013.

Valin, L. C. et al.: Variations of OH radical in an urban plume inferred from NO2 column measurements, Geophys. Res. Lett., 40, 1856-1860, 2013.

Vinken, G. C. M. et al.: Worldwide biogenic soil NOx emissions inferred from OMI NO2 observations, Atmos. Chem. Phys., 14, 10363-10381, 2014.

Vogt, R. et al.: A mechanism for halogen release from sea-salt aerosol in the remote marine boundary layer, Nature, 383, 327-330, 1996.

Wang, Y. et al.: Late-spring increase of trans-Pacific pollution transport in the upper troposphere, Geophys. Res. Lett., 33, L01811, 2006.

Wang, T. et al.: Strong ozone production in urban plumes from Beijing, China, Geophys. Res. Lett., 33, L21806, 2006.

Wang, Y. et al.: Assessing the photochemical impact of snow emissions over Antarctica during ANTCI 2003, Atmos. Environ., 41, 3944-3958, 2007.

Wang, S. et al.: Satellite detection and model verification of NOx emissions from power plants in Northern China, Environ. Res. Lett., 5, 2010.

Wang, M. et al.: Development and validation of a cryogen-free automatic gas chromatograph system (GC-MS/FID) for online measurements of volatile organic compounds, Anal. Methods, 6, 9424–9434, 2014.

Wang, T. et al.: Observations of nitryl chloride and modeling its source and effect on ozone in the planetary boundary layer of southern China, J. Geophys. Res. Atmos., 121, 2476-2489, 2016.

Wang, W. et al.: Evaluating the Governing Factors of Variability in Nocturnal Boundary Layer Height Based on Elastic Lidar in Wuhan, Int. J. Environ. Res. Public Health, 13, 1071, 2016.

Wang, Y. et al.: Observation of atmospheric peroxides during Wangdu campaign 2014 at a rural site in the North China Plain, Atmos. Chem. Phys., 16, 10985-11000, 2016.

Wang, T. et al.: Ozone pollution in China: A review of concentrations, meteorological influences, chemical precursors, and effects, Sci. Total Environ., 575, 1582-1596, 2017.

Wild, O. et al.: Fast-J: Accurate simulation of in- and below-cloud photolysis in tropospheric chemical models, J. Atmos. Chem., 37, 245–282, 2000.

Wu, J. et al.: On the Origin of Surface Ozone Episode in Shanghai over Yangtze River Delta during a Prolonged Heat Wave, Aerosol Air Qual. Res., 17, 2804-2815, 2017.

Xie, R. et al.: Long-term trend and spatial pattern of PM2.5 induced premature mortality in China, Environ. Int., 97, 180-186, 2016.

Xing, J. et al.: Nonlinear response of ozone to precursor emission changes in China: a modeling study using response surface methodology, Atmos. Chem. Phys., 11, 5027-5044, 2011.

Xu, J. et al.: Chemical characteristics of submicron particles at the central Tibetan Plateau: insights from aerosol mass spectrometry, Atmos. Chem. Phys., 18, 427-443, 2018.

Xue, L. et al.: Oxidative capacity and radical chemistry in the polluted atmosphere of Hong Kong and Pearl River Delta region: analysis of a severe photochemical smog episode, Atmos. Chem. Phys., 16, 9891-9903, 2016.

Yang, Q. et al.: NOx emission reduction and its effects on ozone during the 2008 Olympic Games, Environ. Sci. Technol., 45, 6404-6410, 2011.

Yang, M. et al.: Air-sea fluxes of oxygenated volatile organic compounds across the Atlantic Ocean, Atmos. Chem. Phys., 14, 7499-7517, 2014.

Ying, Z. et al.: Sensitivity of ozone concentrations to diurnal variations of surface emissions in Mexico City: A WRF/Chem modeling study, Atmos. Environ., 43, 851-859, 2009.

Young, P. J. et al.: Pre-industrial to end 21st century projections of tropospheric ozone from the Atmospheric Chemistry and Climate Model Intercomparison Project (ACCMIP), Atmos. Chem. Phys., 13, 2063-2090, 2013.

Zeng, T. et al.: Halogen-driven low-altitude O3 and hydrocarbon losses in spring at northern high latitudes, J. Geophys. Res.-Atmos., 111, D17313, 2006.

Zhang, Q. et al.: Asian emissions in 2006 for the NASA INTEX-B mission, Atmos. Chem. Phys., 9, 5131-5153, 2009.

Zhang, G. et al.: Summertime distributions of peroxyacetyl nitrate (PAN) and peroxypropionyl nitrate (PPN) in Beijing: Understanding the sources and major sink of PAN, Atmos. Environ., 103, 289-296, 2015.

Zhang, Y. et al.: Large vertical gradient of reactive nitrogen oxides in the boundary layer: Modeling analysis of DISCOVER-AQ 2011 observations, J. Geophys. Res.-Atmos., 121, 1922-1934, 2016.

Zhang, R. et al.: Enhanced trans-Himalaya pollution transport to the Tibetan Plateau by cut-off low systems, Atmos. Chem. Phys., 17, 3083-3095, 2017.

Zhang, L. et al.: Updated emission inventories of power plants in simulating air quality during haze periods over East China, Atmos. Chem. Phys., 18, 2065-2079, 2018.

Zhang, R. et al.: Comparing OMI-based and EPA AQS in situ NO2 trends: towards understanding surface NOx emission changes, Atmos. Meas. Tech., 11, 3955-3967, 2018.

Zhao, C. and Wang, Y.: Assimilated inversion of NOx emissions over East Asia using OMI NO2 column measurements, Geophys. Res. Lett., 36, L06805, 2009.

Zhao, C. et al.: East China plains: A “basin” of ozone pollution, Environ. Sci. Technol., 43, 1911-1915, 2009a.

Zhao, C. et al.: Summertime impact of convective transport and lightning NOx production over North America: modeling dependence on meteorological simulations, Atmos. Chem. Phys., 9, 4315-4327, 2009b.

Zhao, Y. et al.: Quantifying the uncertainties of a bottom-up emission inventory of anthropogenic atmospheric pollutants in China, Atmos. Chem. Phys., 11, 2295-2308, 2011.

Zhao, B. et al.: NOx emissions in China: historical trends and future perspectives, Atmos. Chem. Phys., 13, 9869-9897, 2013.

Zhao, Y. et al.: Assessment of a high-resolution NOx emission inventory using satellite observations: A case study of southern Jiangsu, China, Atmos. Environ., 190, 135-145, 2018.

Zhao, Y. et al.: Influences of planetary boundary layer mixing parameterization on summertime surface ozone concentration and dry deposition over North China, Atmos. Environ., 218, 116950, 2019.

Zheng, B. et al.: Trends in China's anthropogenic emissions since 2010 as the consequence of clean air actions, Atmos. Chem. Phys., 18, 14095–14111, 2018.

Zhou, Z. et al.: Emission inventory of anthropogenic air pollutant sources and characteristics of VOCs species in Sichuan Province, China, J. Atmos. Chem., 76, 21-58, 2019.